Title: A Surveillance Pathway Senses Leaked Mitochondrial DNA to Activate UPR^{mt} and Promote Longevity

Authors: Yung Wu[1,2,3]* and Hongyun Tang[1,2,3,4]*

[1] College of Life Sciences, Zhejiang University, Hangzhou, 310058, China

[2] State Key Laboratory of Gene Expression, School of Life Sciences, Westlake University, Hangzhou 310024, China

[3] Westlake Laboratory of Life Sciences and Biomedicine, Hangzhou 310024, China

[4] Senior author

*Correspondence: wuyong@westlake.edu.cn; tanghongyun@westlake.edu.cn

Abstract

The mitochondrial unfolded protein response (UPR^{mt}) is a critical mechanism for restoring cellular homeostasis and promoting longevity upon mitochondrial stress. However, the mechanisms that sense specific mitochondrial damage-associated signals and activate UPR^{mt} remain largely unknown. Through a genome-wide RNAi screen in *Caenorhabditis elegans*, we identified the AT-hook protein LIN-15B as a mitochondrial stress sensor that detects leaked mitochondrial DNA (mtDNA) to activate UPR^{mt}. We show that LIN-15B contains a mitochondrial targeting sequence (MTS) and a C-terminal domain with nuclear localization capability. Upon mitochondrial stress, LIN-15B accumulates on the outer mitochondrial membrane (OMM) and utilizes its C-terminal AT-hook domains to directly bind leaked mtDNA, with a preference for the AT-rich D-loop region. This interaction is required for the nuclear translocation of LIN-15B, which occurs independently of the canonical protein import sensor ATFS-1. Nuclear LIN-15B then activates a broad transcriptional program encompassing core UPR^{mt} targets and a unique set of DNA repair genes. This surveillance pathway is critical for preserving mitochondrial network integrity and supporting organismal longevity. Our findings define a mitochondrial surveillance pathway in which LIN-15B senses displaced mtDNA, triggering a protective transcriptional response that promotes longevity, thus revealing a principle of cellular

homeostasis monitoring via the detection of displaced self components.

Mitochondria are essential hubs for cellular energy production, metabolism, and signaling, and their functional decline is a hallmark of aging and age-related diseases [1]. To counteract mitochondrial stress and restore homeostasis, cells have evolved the mitochondrial unfolded protein response (UPR^{mt}), a transcriptional program that selectively upregulates a series of genes, including chaperones and proteases, to restore function and promote longevity [2-4]. In *C. elegans*, ATFS-1, suggested to be a homolog of mammalian ATF5, is known to mediate nuclear transcription in response to mitochondrial protein import defects, providing a well-characterized mechanism of UPR^{mt} regulation [5, 6]. Under normal conditions, ATFS-1 is imported into and degraded within mitochondria; upon mitochondrial protein import defects, it accumulates in the cytosol and translocates to the nucleus, where it collaborates with a suite of chromatin modifiers to activate the protective UPR^{mt} program [4, 5, 7-10].

Although the ATFS-1 pathway offers a robust mechanism for detecting mitochondrial proteostatic imbalances, how cells detect other forms of mitochondrial damage, including metabolic dysfunction, membrane depolarization, and the release of mitochondrial DNA into the cytosol, remains poorly understood. Exposure to these stressors has been shown to induce inflammatory responses [11-13], apoptosis [14], and genomic instability [15, 16], thereby contributing to age-related diseases. However, whether and how these non-protein import-related mitochondrial insults are sensed to activate responses for restoring homeostasis is not well defined.

Here, we hypothesized that cells surveil organellar integrity by recognizing ‘displaced self’, endogenous components that become mislocalized during stress. We identify the AT-hook protein LIN-15B as a mitochondrial stress sensor that monitors mtDNA cytosolic leakage and translocates to the nucleus to trigger UPR^{mt}, functioning independently of ATFS-1. Our findings define a surveillance pathway that translates a potentially harmful signal, leaked mtDNA, to mount a protective, life-extending response. These results suggest that cells employ ‘displaced self’

recognition as a surveillance principle to sense organellar stress and activate specific protective pathways.

A genome-wide screen identifies *lin-15B* as an essential regulator for UPR^{mt} activation

To identify novel regulators of the mitochondrial unfolded protein response (UPR^{mt}), we performed a genome-wide RNAi screen in *C. elegans* harboring the *isp-1(qm150)* mutation, which impairs a subunit of mitochondrial electron transport chain complex III and leads to constitutive activation of the UPR^{mt} reporter *hsp-6p::GFP* [17]. This screen identified that *lin-15B* is required for UPR^{mt} activation, as RNAi knockdown of *lin-15B* strongly abolished reporter activation (Extended Data Fig. 1a).

To validate the role of *lin-15B*, we generated *lin-15B(jef48)*, a *lin-15B* knockout strain, using the CRISPR-Cas9 method. Similar to *atfs-1(gk3094)*, *lin-15B(jef48)* suppressed the upregulation of *hsp-6p::GFP* induced by knockdown of *cco-1*, which encodes cytochrome c oxidase subunit 5B, another component of the electron transport chain commonly targeted to induce mitochondrial stress (Extended Data Fig. 1b, c). Re-expression of LIN-15B under its native promoter in the *lin-15B(jef48)* background restored *cco-1* RNAi-induced UPR^{mt} activation (Fig. 1a, b). Consistently, loss of *lin-15B* suppressed the upregulation of endogenous *hsp-6* transcripts induced by *cco-1* RNAi (Fig. 1c). Notably, compared with RNAi control, *cco-1* RNAi caused severe sterility in *lin-15B* mutants (Fig. 1d), indicating a critical role for *lin-15B* in coping with mitochondrial stress. Although *lin-15B* and *lin-15A* are encoded within a single genomic operon, we found that the requirement for UPR^{mt} activation was specific to *lin-15B*, as UPR^{mt} activation induced by *cco-1* RNAi was not suppressed in *lin-15A(n767)* mutant worms (Extended Data Fig. 1d, e).

We next sought to determine whether *lin-15B* responds only to electron transport chain disruption or acts as a more general regulator of mitochondrial homeostasis in response to impairment of diverse mitochondrial processes. Indeed, loss of *lin-15B* suppressed UPR^{mt} activation triggered by a wide array of mitochondrial insults,

including defects in protein folding (*hsp-6* RNAi), proteostasis (*spg-7* RNAi), ATP synthesis (*atp-1* RNAi), and protein import (*tim-23* RNAi) (Fig. 1e, f). In contrast, *lin-15B* did not substantially participate in the endoplasmic reticulum unfolded protein response (UPR^{ER}), as *lin-15B* RNAi failed to significantly suppress tunicamycin-induced expression of *hsp-4p::GFP* (Extended Data Fig. 1f). Similarly, *lin-15B* is not involved in the heat shock response (HSR), as knockdown of *lin-15B* did not inhibit the induction of *hsp-16.2p::GFP* following heat shock (Extended Data Fig. 1g). Taken together, these data establish a specific role of *lin-15B* in UPR^{mt}, essential for responding to diverse forms of mitochondrial stress.

LIN-15B contains a cryptic MTS and accumulates on the outer mitochondrial membrane upon mitochondrial stress to activate UPR^{mt}

To understand how LIN-15B regulates the UPR^{mt}, we investigated its subcellular localization. In a transgenic worm strain expressing LIN-15B::GFP::Flag under the native *lin-15B* promoter (Is[*lin-15Bp::lin-15B::gfp::flag*]), LIN-15B exhibited clear nuclear localization in embryonic cells (Extended Data Fig. 2a). Similarly, heterologous expression of LIN-15B-GFP in HEK293T cells also revealed prominent nuclear localization (Fig. 2a). To define the regions governing subcellular localization of LIN-15B, we generated a series of N-terminal truncation mutants and expressed them in HEK293T cells. Unexpectedly, deletion of the N-terminal 200 or 300 residues (ΔN200/ΔN300), unmasked a cryptic mitochondrial targeting activity, resulting in prominent colocalization with MitoTracker (Fig. 2a). Further deletion of the N-terminal 350 residues (ΔN350) resulted in robust mitochondrial localization, whereas deletion of the N-terminal 400 residues (ΔN400) abolished mitochondrial localization (Fig. 2a), suggesting that a functional MTS resides within amino acids 351-400. Direct fusion of residues 351-400 to GFP was sufficient to target GFP to mitochondria in both HEK293T cells and worm body wall muscle cells, as indicated

by colocalization with MitoTracker staining and TOM-20::mKate, respectively (Fig. 2b, d). Expression of GFP fused to the corresponding MTS regions in LIN-15B orthologs from *C. remanei* and *C. brenneri* in *C. elegans* body wall muscle also showed co-localization with mitochondria (Fig. 2c, d). Collectively, these results indicate that LIN-15B contains a conserved MTS.

Structural prediction and mutagenesis revealed this MTS consists of two adjacent α-helices that function redundantly; only when both helices were mutated was mitochondrial targeting abolished (Extended Data Fig. 2b, c). Specifically, individual alanine substitutions of the entire first α-helix ($\alpha1^{mut}$), the entire second α-helix ($\alpha2^{mut}$), or the intervening linker region ($linker^{mut}$) still permitted mitochondrial localization when expressed under *myo-3* promoter in worm body wall muscle cells. In contrast, simultaneous mutation of 10 central residues in both helices ($\alpha1/2^{mut}$) completely abolished mitochondrial targeting (Extended Data Fig. 2c). Importantly, neither the full-length LIN-15B carrying the $\alpha1/2^{mut}$ mutation in the MTS ($LIN\text{-}15B^{MTSmut}$) nor the MTS deletion variant ($LIN\text{-}15B^{\Delta MTS}$, lacking residues 351-400) rescued UPR^{mt} activation in *lin-15B(jef48)* upon *cco-1* RNAi treatment (Fig. 2e, f, and Extended Data Fig. 2d, e). These results demonstrate that the bipartite MTS (residues 351–400) is indispensable for LIN-15B to mediate UPR^{mt} activation.

Having demonstrated the essential role of the MTS in UPR^{mt} activation, we next asked whether mitochondrial stress triggers LIN-15B translocation to mitochondria. We employed mitochondrial enrichment followed by western blot analysis to quantitatively evaluate LIN-15B translocation. Mitochondria were affinity-purified from worms carrying *lin-15Bp::lin-15B::flag* and *eft-3p::tomm-20::mKate2::HA* transgenes using anti-HA antibody-conjugated magnetic beads (Fig. 2g). In the control group for mitochondrial purification specificity, 1% Triton X-100 was added to solubilize the mitochondria to confirm that LIN-15B in the mitochondrial fraction was not a result of the non-specific binding of LIN-15B to magnetic beads. Compared to the empty vector (EV) RNAi control, LIN-15B accumulated in purified mitochondria upon *cco-1* RNAi treatment (Fig. 2h). Notably, upon *cco-1* RNAi, the LIN-15B band was upshifted compared with the EV control, and in the mitochondrial

fraction, LIN-15B migrated as the higher-molecular weight form (Fig. 2h), which may suggest post-translational modifications (not further characterized here).

To determine the submitochondrial localization of LIN-15B upon mitochondrial stress, we performed a proteinase K protection assay on freshly isolated mitochondria from *cco-1* RNAi-treated worms. The mitochondrial inner membrane protein ATP-1 (ATP5A) and cytochrome c (Cyt. C) were resistant to proteinase K digestion owing to their protection by the outer mitochondrial membrane. In contrast, like the outer membrane protein TOMM-20, LIN-15B was susceptible to digestion by proteinase K (Fig. 2i), indicating that LIN-15B localizes to the outer mitochondrial membrane (OMM). Collectively, LIN-15B responds to mitochondrial stress by accumulating on the outer mitochondrial membrane.

LIN-15B senses leaked mtDNA upon mitochondrial stress

The stress-induced accumulation of LIN-15B on the outer mitochondrial membrane, coupled with its possession of DNA-binding domains (a THAP domain and AT-hooks), led us to hypothesize that LIN-15B acts as a mitochondrial damage sensor by detecting mtDNA potentially released during mitochondrial stress. Supporting this idea, we found that biotinylated mtDNA precipitated Flag-tagged LIN-15B, but not the Flag-tagged GFP negative control, from transfected HEK293T lysates (Fig. 3a), indicating LIN-15B is capable of binding to mtDNA. To determine whether mitochondrial stress induces mtDNA leakage *in vivo* in worms, we quantified cytosolic mtDNA by qPCR targeting the mtDNA-encoded genes ND1, ND2, 12S rRNA, and COX2. *cco-1* RNAi-induced mitochondrial stress resulted in a significant increase in cytosolic mtDNA level compared with the RNAi control, indicating mtDNA release into the cytosol (Fig. 3b). To assess whether LIN-15B binds to the mtDNA *in vivo*, worms expressing LIN-15B::GFP::Flag were subjected to formaldehyde crosslinking, followed by Flag immunoprecipitation and qPCR analyses of the mtDNA genes. Compared to the RNAi control, *cco-1* RNAi-induced mitochondrial stress significantly increased the binding of LIN-15B to mtDNA (Fig.

3c). Consistent with LIN-15B's recruitment to the OMM and its ability to bind mtDNA, immunogold transmission electron microscopy (TEM) using an antibody against dsDNA revealed DNA signal in the cytosol and notably on the cytosolic face of the OMM in intestinal cells upon *cco-1* RNAi-induced mitochondrial stress (Fig. 3d). Taken together, these findings indicate that mitochondrial stress leads to mtDNA leakage, which is specifically detected by LIN-15B.

LIN-15B binds the mtDNA D-loop via AT-hook motifs to mediate UPR^{mt}

To map the mtDNA-binding domain of LIN-15B, we evaluated the binding capabilities of LIN-15B truncations. Neither deletion of the THAP domain (residues 1135-1209) nor alanine substitution of the four conserved CCCH zinc finger residues (C1139A, C1142A, C1185A, and H1188A; hereafter referred to as LIN-15B^{THAP4A}) affected mtDNA binding (Fig. 3e and Extended Data Fig. 3). In contrast, deletion of the C-terminal region (residues 1221-1440) completely abolished mtDNA binding (Fig. 3e). The C-terminal region contains two AT-hooks, motifs typically known to bind AT-rich DNA, suggesting that LIN-15B selectively targets AT-rich regions within mtDNA rather than binding indiscriminately. To test this prediction, we performed pull-down assays using four biotinylated mtDNA fragments with varying AT content, derived from the 12S rRNA (DNA-1), ND1 (DNA-2), D-loop (DNA-3), and 16S rRNA (DNA-4) loci (Fig. 3f). Notably, the D-loop is the regulatory region of the mitochondrial genome and is characterized by extremely high AT content (93% across the full D-loop region). LIN-15B exhibited a marked binding preference for AT-rich fragments, with the strongest interaction observed for the D-loop fragment (DNA-3). In contrast, no binding was detected to the DNA-1 and DNA-2 fragments, which have relatively low AT content (Fig. 3f). Therefore, this suggests a specific and targeted recognition event. Importantly, re-expression of a C-terminally truncated LIN-15B lacking the AT-hook motifs, and thus defective in mtDNA binding, failed to rescue *cco-1* RNAi-induced UPR^{mt} activation in *lin-15B(jef48)* animals (Fig. 3g, h). Together,

these data suggest that the C-terminal AT-hooks domain of LIN-15B mediates its interaction with AT-rich mtDNA regions, particularly the D-loop, to promote UPR^{mt} activation.

Mitochondrial stress induces nuclear translocation of LIN-15B in a manner dependent on its mitochondrial localization and mtDNA binding

We then investigated how LIN-15B mediates UPR^{mt} activation upon mitochondrial localization and binding to mtDNA. Although the THAP domain was dispensable for mtDNA binding, the LIN-15B^{THAP4A} mutant failed to rescue UPR^{mt} activation in *lin-15B(jef48)* animals (Extended Data Fig. 4a, b). Previous studies have shown that THAP domain-containing proteins typically function as transcriptional regulators in the nucleus [18-20], suggesting a potential nuclear function for LIN-15B as well. In contrast to its constitutive nuclear localization in embryonic cells, LIN-15B was largely absent from the nucleus in adult intestinal cells under basal conditions (Extended Data Fig. 2a, Extended Data Fig. 5a, b). However, mitochondrial stress robustly induced LIN-15B translocation to the nucleus in intestinal cells (Extended Data Fig. 5a, b).

Next, we aimed to determine whether outer mitochondrial membrane recruitment and mtDNA binding are required for mitochondrial stress-induced nuclear entry of LIN-15B. First, to test the role of LIN-15B mitochondrial localization in regulating its nuclear localization, we examined variants of LIN-15B with either a mutated MTS or deleted MTS. Deletion or mutation of the MTS in LIN-15B completely blocked LIN-15B translocation to the nucleus in intestinal cells in the presence of *cco-1* RNAi (Fig. 4a, b). It is important to note that the deletion or mutation of the MTS does not disrupt the nuclear localization sequence (NLS) of LIN-15B. Using worm embryonic cells, in which LIN-15B is constitutively localized to the nucleus (Extended Data Fig. 2a), we mapped the NLS to the C-terminal region (residues 1221–1440). In contrast, the N-

terminal fragment (residues 1–1220) localizes to the cytoplasm (Extended Data Fig. 5c). Therefore, the NLS and the MTS (residues 351–400) reside in distinct regions of LIN-15B. These results suggest that LIN-15B recruitment to mitochondria is required for its nuclear entry upon mitochondrial stress.

Furthermore, we tested the requirement of mtDNA-binding for nuclear translocation by examining LIN-15B variants with deleted AT-hook motifs. The C-terminal region (residues 1221-1440) contains two AT-hook motifs. Deletion of the AT-hook1 (residues 1317-1328) markedly inhibited nuclear translocation in intestinal cells upon *cco-1* RNAi treatment, whereas deletion of AT-hook2 (residues 1418-1429) exerted a modest inhibitory effect (Fig. 4c, d). Importantly, neither deletion affects its constitutive nuclear localization in worm embryonic cells (Extended Data Fig. 5d), proving they specifically disrupt the stress-induced nuclear translocation. These data indicate that mitochondrial stress-induced nuclear translocation of LIN-15B requires mtDNA binding via the AT-hook motifs, with AT-hook1 playing the primary role and AT-hook2 likely providing a supportive contribution. Notably, deletion of the entire C-terminal region (residues 1221-1440), which removes the two AT-hook motifs, did not prevent mitochondrial recruitment of LIN-15B upon *cco-1* RNAi-induced mitochondrial stress (Fig. 4e), suggesting that mitochondrial recruitment of LIN-15B occurs independently of mtDNA binding. Taken together, these results support a two-step mechanism: LIN-15B first translocates to the outer mitochondrial membrane (OMM) to bind leaked mtDNA, and this interaction subsequently facilitates its nuclear translocation.

LIN-15B nuclear translocation is independent of *atfs-1* and upregulates DNA repair genes

Next, we investigated whether the nuclear entry of LIN-15B depends on canonical UPR^{mt} regulators. Like LIN-15B, the transcription factor ATFS-1 harbors both an MTS and an NLS. During mitochondrial stress, ATFS-1 senses mitochondrial protein import defects via its weak MTS and enters the nucleus mediated by its NLS [5, 21].

Strikingly, *atfs-1* knockdown does not inhibit *cco-1* RNAi-induced nuclear translocation of LIN-15B; instead, it enhances it (Fig. 5a, b). LIN-65 is a chromatin modifier that acts as another regulator of UPR^{mt}, translocating to the nucleus in an ATFS-1-independent manner during mitochondrial stress to facilitate chromatin remodeling and UPR^{mt} activation[4]. Similar to *atfs-1* RNAi, loss of *lin-65* also enhances, but does not inhibit, LIN-15B nuclear translocation (Extended Data Fig. 6a, b). These data indicate that the LIN-15B-mediated mtDNA sensing mechanism operates in parallel with the ATFS-1- and LIN-65-dependent pathways to activate UPR^{mt}.

To elucidate the role of LIN-15B-mediated responses, we characterized the transcriptional profiles regulated by LIN-15B and ATFS-1, which serve as sensors for mtDNA leakage and mitochondrial protein import defects, respectively. Transcriptomic analyses revealed that induction of 1,711 out of 1,998 mitochondrial stress-responsive genes by *cco-1* RNAi required both *lin-15B* and *atfs-1* (Fig. 5c, d, and Extended Data Table 1), indicating that full activation of UPR^{mt} depends on the coordinated function of these two pathways. Intriguingly, gene ontology (GO) enrichment analysis of the 99 mitochondrial stress-induced genes regulated by *lin-15B* but not *atfs-1* revealed genes enriched in pathways related to DNA repair and DNA replication (Fig. 5c, e, Extended Data Table 2 and 3). These results align with the role of LIN-15B as a sensor of mtDNA leakage. Since leaked mtDNA may act as a signal of DNA damage or intracellular oxidative stress, LIN-15B's activation of DNA repair genes may serve as a protective mechanism against genotoxic threats arising from mitochondrial dysfunction. These results indicate that LIN-15B broadly regulates UPR^{mt} transcription and additionally governs a distinct gene expression program enriched for genome maintenance pathways.

The LIN-15B pathway is essential for mitochondrial integrity and organismal longevity

The physiological significance of this mtDNA-LIN-15B surveillance pathway is

underscored by the severe consequences of disrupting *lin-15B*. Genetic ablation of *lin-15B* caused severe cellular and organismal defects even in the absence of mitochondrial stress. Transmission electron microscopy (TEM) analyses of intestinal cells revealed that *lin-15B* mutants exhibited fragmented and swollen mitochondria (Fig. 5f and Extended Data Fig. 7), indicating a critical role of LIN-15B in sustaining mitochondrial network integrity under basal conditions. Consistently, *lin-15B* mutants exhibited a shortened lifespan (Fig. 5g, Extended Data Table 4), highlighting an essential role of LIN-15B in maintaining mitochondrial homeostasis. Moreover, LIN-15B was essential for the adaptive response to stress. It has been well known that mild mitochondrial stress induced by *cco-1* RNAi during development extends lifespan [3, 22]. We found that *lin-15B* deficiency inhibited lifespan extension caused by *cco-1* RNAi (Fig. 5h, Extended Data Table 4). These results, together with severe sterility of *lin-15B* mutant under mitochondrial stress (Fig. 1d), indicated that LIN-15B mediated surveillance pathway is essential for maintaining mitochondrial homeostasis, ensuring normal lifespan, and enabling adaptive longevity.

Discussion

In this study, we identify LIN-15B as a molecular sensor that directly detects cytosolic mtDNA. Upon mitochondrial stress, LIN-15B is recruited to the mitochondrial outer membrane, where it recognizes leaked mtDNA via the AT-hook domain. This interaction promotes its nuclear import, enabling it to drive the transcription of UPR^{mt} and promote longevity (Fig. 5i). Our discovery of LIN-15B as an mtDNA leakage sensor demonstrates that mitochondrial stress surveillance can operate through specialized detectors for specific forms of damage-associated signals.

Cytosolic mtDNA is well established as a proinflammatory signal in mammals that activates cGAS-STING to drive aging and neurodegenerative diseases [13, 14, 23-25]. However, our research reveals that in *C. elegans*, LIN-15B interprets cytosolic mtDNA as a cellular alarm signal to activate a protective response and restore homeostasis. This paradox suggests potential context-dependent roles of cytosolic

mtDNA, where the same molecule may be pathogenic or beneficial depending on the cellular machinery it engages. Consistent with this view, protective cellular responses linked to genome maintenance elicited by cytosolic mtDNA have also been observed under specific conditions in mammalian systems [26]. Nevertheless, in higher organisms, cytosolic mtDNA has predominantly been studied in the context of innate immune activation, which may bias the observed outcomes toward inflammation. In contrast, *C. elegans* lacks mammalian-like innate inflammatory pathways, providing a system in which alternative, protective mtDNA-responsive mechanisms can be uncovered. The key functional domains of LIN-15B (THAP and AT-hook) possess homologs in mammals. This domain conservation raises the possibility that a protective mtDNA-sensing mechanism may also exist in higher organisms. The distribution of these domains across multiple mammalian proteins suggests evolutionary divergence, in which LIN-15B's roles may be partitioned among cooperating factors. Future studies should exploit the mechanistic insights from *C. elegans* to re-examine cytosolic mtDNA response in mammals. The domain conservation in mammalian proteins provides molecular entry points for this investigation.

Our discovery of LIN-15B as a sensor for cytosolic mtDNA suggests a previously unrecognized principle of cellular surveillance: cells can monitor organelle homeostasis through the detection of displaced organelle molecular patterns (DOMPs). This concept is supported by emerging evidence of displaced organelle components acting as signaling molecules for cellular surveillance. For example, the study in mammals revealed that during mitochondrial misfolding stress, the release of mitochondrial reactive oxygen species (mtROS) together with cytosolic accumulation of mitochondrial protein precursors trigger UPR^{mt} via the DNAJA1–HSF1 axis [27]. Similarly, exposure of sphingomyelin on damaged lysosomes recruiting TECPR1 for autophagy [28, 29], and galectin-8 binding exposed glycans on damaged endosomes for selective autophagy [30]. We anticipate that exploration into DOMPs recognition across other organelles will uncover previously uncharacterized pathways of cellular defense, with broad implications for neurodegenerative diseases, metabolic disorders,

and aging research.

Fig. 1 | *lin-15B* is required for UPR^{mt} activation and mitochondrial stress resistance.

a, *lin-15B(jef48)* suppressed *cco-1* RNAi-induced *hsp-6p::GFP* activation, and integrated expression of *lin-15Bp::lin-15B::flag* restored *hsp-6p::GFP* induction in *lin-15B(jef48)* animals. Scale bar, 200 µm.

b, Quantification of *hsp-6p::GFP* fluorescence intensity shown in (**a**). *n* = 30 worms for each condition from 3 independent biological experiments.

c, *lin-15B* and *atfs-1* were required for induction of endogenous *hsp-6* mRNA upon *cco-1* RNAi-induced mitochondrial stress. *n* = 3 biologically independent experiments.

d, *lin-15B* mutants exhibited synthetic sterility in response to *cco-1* RNAi. Wild-type (WT) and *lin-15B(jef48)* animals were treated with EV or *cco-1* RNAi. Day 1 adult animals were imaged. A representative image from one of three biologically independent experiments is shown. Scale bar, 1 mm.

e, Knockdown of *hsp-6* (protein folding), *spg-7* (protease), *atp-1* (ATP synthesis), and *tim-23* (protein import) induced upregulation of *hsp-6p::GFP* in a *lin-15B*-dependent manner. Scale bar, 200 µm.

f, Quantification of *hsp-6p::GFP* fluorescence intensity shown in (**e**). *n* = 30 worms for each condition from 3 independent biological experiments.

For all statistics, data are presented as mean ± SEM. P values in (**b**), (**c**), and (**f**) were calculated using two-way ANOVA with Šidák's multiple-comparisons test.

Fig. 2 | Mitochondrial stress-induced accumulation of LIN-15B on the outer mitochondrial membrane is required for UPR^{mt} activation.

a, In HEK293T cells, full-length LIN-15B fused to GFP localized to the nucleus. Deletion of the N-terminal 200, 300, or 350 residues showed colocalization with MitoTracker, while deletion of the N-terminal 400 residues showed nuclear localization. Scale bar, 10 µm.

b, In HEK293T cells, LIN-15B residues 351-400 fused to GFP (351-400-GFP)

showed colocalization with MitoTracker. Scale bar, 10 μm.

c, Sequence alignments identified corresponding mitochondrial targeting sequence (MTS) regions in LIN-15B orthologs from *C. remanei* and *C. brenneri*. Protein sequences were aligned using the ClustalW algorithm, and alignment result was visualized with ESPript 3.0.

d, Extrachromosomal expression of *myo-3p::lin-15B 351-400::gfp, myo-3p::lin-15B (C. brenneri) 344-393::gfp,* and *myo-3p::lin-15B (C. remanei) 338-387::gfp* in *myo-3p::tom-20::mKate2::HA* transgenic *C. elegans* resulted in co-localization of the LIN-15B fragments with the mitochondrial marker TOM-20::mKate2::HA in body-wall muscle cells. Scale bar, 10 μm.

e, The *LIN-15B*^{MTSmut} transgene failed to rescue the upregulation of *hsp-6p::GFP* induced by *cco-1* RNAi. Wild-type (WT), *lin-15B(jef48)* and two integrated rescue strains (Is[*lin-15Bp::lin-15B::flag*]; *lin-15B(jef48)* and mitochondrial-targeting-defective mutant *Is[lin-15Bp::lin-15B*^{MTSmut}*::flag*]; *lin-15B(jef48)*) each carrying the *hsp-6p::GFP* reporter, were treated with EV or *cco-1* RNAi. Scale bar, 200 μm.

f, Quantification of *hsp-6p::GFP* fluorescence intensity shown in (**e**). n = 30 worms for each condition from 3 independent biological experiments. P values were calculated using two-way ANOVA with Šidák's multiple-comparisons test. Error bars indicate mean ± SEM.

g, Schematic of mitochondrial purification process used in (**h**).

h, *cco-1* RNAi promoted LIN-15B recruitment to mitochondria. Affinity-purified mitochondria from the integrated strain Is[*lin-15Bp::lin-15B::flag*]; Si[*eft-3p::tomm-20::mKate2::HA*] treated with empty vector (EV) or *cco-1* RNAi were analyzed. Triton X-100 solubilization of mitochondria served as a control to confirm the purity of isolated mitochondria and rule out non-specific binding of LIN-15B to beads during the assay. The upward shift of LIN-15B bands, likely resulting from post-translational modifications, is indicated by red arrows.

i, Western blot showing that mitochondria-localized LIN-15B is susceptible to proteinase K digestion. Mitochondria from *cco-1* RNAi-treated Is[*lin-15Bp::lin-15B::flag*]; Si[*eft-3p::tomm-20::mKate2::HA*] animals were isolated and then treated

with proteinase K, followed by western blot analysis to detect LIN-15B.

Fig. 3 | LIN-15B senses mitochondrial stress by binding to leaked cytosolic mtDNA via its AT-hook domain.

a, Biotinylated mtDNA pulled down Flag-LIN-15B, but not the Flag-GFP control. Pull-down assays using a biotinylated mtDNA fragment (~11 kb) were performed on lysates from HEK293T cells expressing either Flag-LIN-15B or Flag-GFP (negative control).

b, qPCR analysis revealed an increased mtDNA release into the cytosol upon *cco-1* RNAi-induced mitochondrial stress. Cytosolic DNA was extracted from EV- or *cco-1* RNAi-treated worms. n = 3 biologically independent experiments, P values were calculated using Welch's t test.

c, Formaldehyde-crosslinking followed by Flag immunoprecipitation and qPCR analysis of mtDNA-encoded genes (ND1, ND2, 12S rRNA, and COX-2). *cco-1* RNAi-induced mitochondrial stress enhanced LIN-15B binding to mtDNA *in vivo*. The experiments were performed in empty vector (EV)- or *cco-1* RNAi-treated Is[*lin-15Bp::lin-15B::gfp::flag*] transgene worms. n = 3 biologically independent experiments, P values were calculated using two-way ANOVA with Šidák's multiple-comparisons test.

d, Immunogold labeling (anti-DNA antibody) combined with TEM shows mtDNA (black dots, arrows) leaking from a compromised mitochondrion (dashed line) in a *cco-1* RNAi-treated animal. Bottom-left numbers indicate the percentage of gold particles localized outside mitochondria (outside/total; EV: n = 90; *cco-1* RNAi: n = 224). Fisher's exact test (two-sided), $P < 0.0001$. Scale bar, 200 nm.

e, DNA pull-down assay demonstrating that the C-terminal AT-hook domain is required for LIN-15B to bind mtDNA. Pull-down assays using a biotinylated mitochondrial DNA fragment (~11 kb) were performed on lysates from HEK293T cells expressing Flag-LIN-15B, Flag-LIN-15B$^{\Delta 1135\text{-}1209}$ (THAP-domain deletion), or Flag-LIN-15B$^{\Delta 1221\text{-}1440}$ (AT-hooks deletion).

f, DNA pull-down assays showing that LIN-15B binds to AT-rich region of the

mitochondrial genome. Left: western blot. Right: Schematic of the four mtDNA fragments used. Pull-down assays were performed on lysates from HEK293T cells expressing Flag-LIN-15B using four biotinylated DNA fragments from distinct regions of mtDNA (left).

g, The LIN-15B$^{\Delta 1221\text{-}1440}$ mutant lacking the C-terminal AT-hooks domain failed to rescue the *hsp-6p::GFP* induction upon *cco-1* RNAi. Wild-type, *lin-15B(jef48)*, and two integrated rescue strains (Is[*lin-15Bp::lin-15B::flag*]; *lin-15B(jef48)* and Is[*lin-15Bp::lin-15B$^{\Delta 1221\text{-}1440}$::flag*]; *lin-15B(jef48)*) each carrying the *hsp-6p::GFP* reporter, were treated with EV or *cco-1* RNAi. Scale bar, 200 µm.

h, Quantification of *hsp-6p::GFP* fluorescence intensity shown in (**g**). *n* = 30 worms per condition from 3 independent biological experiments. P values were calculated using two-way ANOVA with Šidák's multiple-comparisons test.

For all graphs, data are presented as mean ± SEM. Representative western blots from one of three biologically independent experiments are shown in (**a**), (**e**), and (**f**).

Fig. 4 | mitochondrial stress induced nuclear translocation of LIN-15B requires both mitochondrial targeting and mtDNA binding.

a, Nuclear translocation of LIN-15B in intestinal cells induced by *cco-1* RNAi is dependent on an intact MTS. Three integrated strains (Is[*lin-15Bp::lin-15B::gfp::flag*], Is[*lin-15Bp::lin-15B^{MTSmut}::gfp::flag*], and Is[*lin-15Bp::lin-15B$^{\Delta MTS}$::gfp::flag*]) in an *eft-3p::tdTomato::H2B* nuclear marker background were treated with EV or *cco-1* RNAi. White arrows indicate representative co-localization of LIN-15B with intestinal cell nuclei. Scale bar, 50 µm.

b, Quantification of mean nuclear GFP fluorescence intensity in (**a**). *n* = 18 worms per condition from 3 independent biological experiments.

c, Nuclear translocation of LIN-15B in intestinal cells induced by *cco-1* RNAi depended on AT-hook 1 and partially depended on AT-hook 2. Three integrated strains (Is[*lin-15Bp::lin-15B::gfp::flag*], Is[*lin-15Bp::lin-15B$^{\Delta AT\text{-}hook1}$::gfp::flag*], and Is[*lin-15Bp::lin-15B$^{\Delta AT\text{-}hook2}$::gfp::flag*]) in an *eft-3p::tdTomato::H2B* nuclear marker

background were treated with EV or *cco-1* RNAi. AT-hook1: residues 1317-1328; AT-hook2: residues 1418-1429. White arrows indicate representative co-localization of LIN-15B with intestinal cell nuclei. Scale bar, 50 µm.

d, Quantification of mean nuclear GFP fluorescence intensity in (**c**). *n* = 18 worms per condition from 3 independent biological experiments.

e, Deletion of the C-terminal region (residues 1221-1440) containing the AT-hooks did not prevent the stress-induced recruitment of LIN-15B to mitochondria. Affinity-purified mitochondria from the Is[*lin-15Bp::lin-15B::flag*]; Si[*eft-3p::tomm-20::mKate2::HA*] and Is[*lin-15Bp::lin-15B*$^{\Delta 1221\text{-}1440}$*::flag*]; Si[*eft-3p::tomm-20::mKate2::HA*]) treated with empty vector (EV) or *cco-1* RNAi were analyzed. The upward shift of LIN-15B bands, likely resulting from post-translational modifications, is indicated by red arrows. A representative result from one of three biologically independent experiments is shown.

P values in (**b**) and (**d**) were calculated using two-way ANOVA with Šidák's multiple-comparisons test. Error bars indicate mean ± SD.

Fig. 5 | LIN-15B defines a parallel mitochondrial surveillance pathway that activates core UPR^{mt} genes and a distinct set of genes involved in DNA repair.

a, Knockdown of *atfs-1* did not prevent *cco-1* RNAi-induced nuclear translocation of LIN-15B. White arrows indicate representative co-localization of LIN-15B with intestinal cell nuclei. Scale bar, 50 µm.

b, Quantification of mean nuclear GFP fluorescence intensity in (**a**). *n* = 18 worms per condition from 3 independent biological experiments. P values were calculated using one-way ANOVA with Tukey's multiple-comparison test. Error bars indicate mean ± SD.

c, Venn diagram comparing genes transcriptionally upregulated by *cco-1* RNAi in N2 wild-type, *atfs-1 (gk3094)*, and *lin-15B(jef48)* animals, revealing distinct and overlapping gene sets controlled by each factor. The data were obtained by RNAseq analyses.

d, Heatmap visualizing the transcription patterns of mitochondrial stress-induced

genes across the indicated genotypes and conditions. N2 (wild-type), *atfs-1 (gk3094)*, and *lin-15B(jef48)* animals under EV or *cco-1* RNAi conditions were analyzed by RNAseq.

e, Gene Ontology (GO) analysis reveals that the 99 LIN-15B-dependent genes are predominantly enriched for DNA repair related processes.

f, Representative TEM images showing that *lin-15B(jef48)* mutants display swollen and disorganized mitochondrial morphology in intestinal cells. Representative mitochondria are indicated by white arrows. *n* = 4 animals per genotype. Scale bar, 1 µm. For additional electron microscopy fields, see Extended Data Fig. 7**.**

g, Lifespan analysis showing that *lin-15B(jef48)* mutation reduces normal lifespan. *n* = 300 worms from 3 biological replicates. See Extended Data Table 4 for lifespan statistics.

h, Graphs showing that the lifespan extension conferred by *cco-1* RNAi is suppressed in by *lin-15B(jef48)* mutation, indicating that LIN-15B is required for the beneficial effects of mild mitochondrial stress. *n* = 300 worms from 3 biological replicates. See Extended Data Table 4 for statistics.

i, Working model illustrating how LIN-15B acts as a sensor for leaked mtDNA upon mitochondrial stress, defining a surveillance pathway enabling UPR^{mt} activation, transcriptional upregulation of DNA repair-related genes and adaptive longevity.

Extended Data Fig. 1 | *lin-15B* is specifically required for UPR^{mt} activation.

a, Representative micrographs showing that *lin-15B* RNAi inhibits *isp-1(qm150)*-induced *hsp-6p::GFP*. Scale bar, 200 µm.

b, Representative micrographs showing that like *atfs-1*, *lin-15B* is required for *hsp-6p::GFP* induction upon *cco-1(RNAi)*. The N2 wild-type, *atfs-1(gk3094)*, and *lin-15B(jef48)* animals, each carrying the *hsp-6p::GFP* reporter, were treated with EV or *cco-1* RNAi. Scale bar, 200 µm.

c, Quantification of *hsp-6p::GFP* fluorescence intensity shown in **(b)**. *n* = 30 worms per condition from 3 independent biological experiments.

d, Representative micrographs showing that the *lin-15A* is not required for *cco-1*

RNAi-induced *hsp-6p::GFP* activation. Wild-type and *lin-15A (n767)* animals, each carrying the *hsp-6p::GFP* reporter, were treated with EV or *cco-1* RNAi. Scale bar, 200 µm.

e, Quantification of *hsp-6p::GFP* fluorescence intensity shown in (**d**). *n* = 30 worms per condition from 3 independent biological experiments.

f, Representative micrographs showing that *lin-15B* is dispensable for the ER Unfolded Protein Response (UPR^{ER}). Unlike the positive control *xbp-1* RNAi, *lin-15B* RNAi fails to block the induction of *hsp-4p::GFP* by tunicamycin. Scale bar, 200 µm.

g, Representative micrographs showing that *lin-15B* is dispensable for the Heat Shock Response (HSR). Unlike the positive control *hsf-1* RNAi, *lin-15B* RNAi fails to block the induction of *hsp-16.2p::GFP* following heat shock. Scale bar, 200 µm.

P values in (**c**) and (**e**) were calculated using two-way ANOVA with Šidák's multiple-comparisons test. Error bars indicate mean ± SEM.

Extended Data Fig. 2 | Residues 351-400 of LIN-15B form two α-helical motifs that function redundantly in mitochondrial targeting.

a, Representative micrographs showing that in embryonic cells, full-length LIN-15B::GFP is predominantly localized to the nucleus. Extrachromosomal expression of *lin-15Bp::lin-15B::gfp* was analyzed in the embryos. White dashed lines indicate individual nuclei. Scale bar, 10 µm.

b, The predicted structure of the LIN-15B MTS (residues 351-400) by AlphaFold2 consists of two adjacent α-helices (α1 and α2).

c, Extrachromosomal expression of the mutant 351-400 MTS constructs (*myo-3p:: α1^{mut}::gfp*, *myo-3p:: linker^{mut}::gfp*, *myo-3p::α2^{mut}::gfp*, and *myo-3p:: α1/2^{mut}::gfp*) in *myo-3p::tom-20::mKate2::HA* transgenic worms revealed that each of the two adjacent α-helices was capable of targeting mitochondria independently (left). The amino acid sequences of α1^{mut}, linker^{mut}, α2^{mut}, and α1/2^{mut} are shown on the right. Scale bar, 10 µm.

d, Representative micrographs showing that a transgene expressing LIN-15B with a complete MTS deletion (ΔMTS) fails to rescue the *hsp-6p::GFP* induction defect in

lin-15B(jef48) mutants. Wild-type, *lin-15B(jef48)*, and Is[*lin-15Bp::lin-15B*$^{\Delta MTS}$*::flag*]; *lin-15B(jef48)* strains, each carrying the *hsp-6p::GFP* reporter, were treated with EV or *cco-1* RNAi. Scale bar, 200 μm.

e, Quantification of *hsp-6p::GFP* fluorescence intensity shown in (**d**). *n* = 30 worms per condition from 3 independent biological experiments. P values were calculated using two-way ANOVA with Šidák's multiple-comparisons test. Error bars indicate mean ± SEM.

Extended Data Fig. 3 | The THAP domain is not required for LIN-15B to interact with mtDNA.

A DNA pull-down assay and the resulting western blot shows that disrupting the THAP domain does not impair the ability of LIN-15B to bind mtDNA. The DNA pull-down assay was performed using a biotinylated mitochondrial DNA fragment (~11 kb) and lysates from HEK293T cells expressing either wild-type Flag-LIN-15B or a THAP-domain mutant (LIN-15B$^{\mathrm{THAP4A}}$: C1139A, C1142A, C1185A, and H1188A). Representative result from one of three biologically independent experiments is shown.

Extended Data Fig. 4 | The THAP domain is required for LIN-15B to mediate UPR$^{\mathbf{mt}}$ activation.

a, The LIN-15B$^{\mathit{THAP4A}}$ mutant (C1139A, C1142A, C1185A, and H1188A) failed to rescue the *hsp-6p::GFP* induction upon *cco-1* RNAi. Wild-type, *lin-15B(jef48)*, and two integrated rescue strains (Is[*lin-15Bp::lin-15B::flag*]; *lin-15B(jef48)* and the THAP-domain mutant Is[*lin-15Bp::lin-15B*$^{\mathit{THAP4A}}$*::flag*]; *lin-15B(jef48)*) each carrying the *hsp-6p::GFP* reporter, were treated with EV control or *cco-1* RNAi. Scale bar, 200 μm.

b, Quantification of *hsp-6p::GFP* fluorescence intensity shown in (**a**). *n* = 30 worms per condition from 3 independent biological experiments. P values were calculated using two-way ANOVA with Šidák's multiple-comparisons test. Error bars indicate mean ± SEM.

Extended Data Fig. 5 | LIN-15B translocates to the nucleus in response to mitochondrial stress.

a, Representative micrographs show that *cco-1* RNAi induced nuclear translocation of LIN-15B. LIN-15B translocation was analyzed by using the integrated Is[*lin-15Bp::lin-15B::gfp::flag*] transgenes. White arrows indicate representative co-localization of LIN-15B with intestinal cell nuclei. Scale bar, 50 µm.

b, Quantification of mean intensity of nuclear GFP fluorescence shown in (**a**). *n* = 18 worms per condition from 3 independent biological experiments. P value was calculated using Welch's t test. Error bars indicate mean ± SD.

c, Extrachromosomal expression of *lin-15Bp::lin-15B*$^{1\text{-}1220}$*::gfp* and *lin-15Bp::lin-15B*$^{1221\text{-}1440}$*::gfp* showed that LIN-15B (1-1220) was localized in cytoplasm and LIN-15B (1221-1440) was localized to the nucleus in embryonic cells. White dashed lines indicate individual nuclei. Scale bar, 10 µm.

d, Extrachromosomal expression of *lin-15Bp::lin-15B::gfp*, *lin-15Bp::lin-15B*$^{\Delta AT\text{-}hook1}$*::gfp*, and *lin-15Bp::lin-15B*$^{\Delta AT\text{-}hook2}$*::gfp* revealed that deletion of AT-hook1 (residues 1317-1328) or AT-hook2 (residues 1418-1429) did not abrogate nuclear localization in embryonic cells. White dashed lines indicate individual nuclei. Scale bar, 10 µm.

Extended Data Fig. 6 | Nuclear translocation of LIN-15B upon mitochondrial stress is independent of *lin-65*.

a, *lin-65* is not required for *cco-1* RNAi-induced nuclear translocation of LIN-15B. White arrows indicate representative co-localization of LIN-15B with intestinal cell nuclei. Scale bar, 50 µm.

b, Quantification of mean intensity of nuclear GFP fluorescence shown in (**a**). *n* = 18 worms per condition from 3 independent biological experiments. P values were calculated using two-way ANOVA with Tukey's multiple-comparisons test. Error bars indicate mean ± SD.

Extended Data Fig. 7 | *lin-15B* deficiency leads to swollen and fragmented mitochondria in adult intestinal cells.

Transmission electron micrographs show that mitochondria in the intestinal cells of *lin-15B* mutants are swollen and disorganized under normal conditions, relative to wild-type N2 animals. n = 4 animals per genotype. Two representative images are shown per animal. Scale bar, 1 μm.

1. Shen, K., et al., Mitochondria as Cellular and Organismal Signaling Hubs. *Annu Rev Cell Dev Biol*, 2022. **38**: p. 179–218.
2. Zhao, Q., et al., A mitochondrial specific stress response in mammalian cells. T*he EMBO Journal*, 2002. **21**(17): p. 4411–4419–4419.
3. Durieux, J., S. Wolff, and A. Dillin, The cell-non-autonomous nature of electron transport chain-mediated longevity. *Cell*, 2011. **144**(1): p. 79–91.
4. Tian, Y., et al., Mitochondrial Stress Induces Chromatin Reorganization to Promote Longevity and UPR(mt). *Cell*, 2016. **165**(5): p. 1197–1208.
5. Nargund, A.M., et al., Mitochondrial import efficiency of ATFS-1 regulates mitochondrial UPR activation. *Science*, 2012. **337**(6094): p. 587–90.
6. Fiorese, C.J., et al., The Transcription Factor ATF5 Mediates a Mammalian Mitochondrial UPR. *Curr Biol*, 2016. **26**(15): p. 2037–2043.
7. Merkwirth, C., et al., Two Conserved Histone Demethylases Regulate Mitochondrial Stress-Induced Longevity. *Cell*, 2016. **165**(5): p. 1209–1223.
8. Shao, L.W., et al., Histone deacetylase HDA-1 modulates mitochondrial stress response and longevity. *Nat Commun*, 2020. **11**(1): p. 4639.
9. Zhu, D., et al., NuRD mediates mitochondrial stress-induced longevity via chromatin remodeling in response to acetyl-CoA level. *Sci Adv*, 2020. **6**(31): p. eabb2529.
10. Li, T.Y., et al., The transcriptional coactivator CBP/p300 is an evolutionarily conserved node that promotes longevity in response to mitochondrial stress. *Nat Aging*, 2021. **1**(2): p. 165–178.
11. Yu, Y.R., et al., Disturbed mitochondrial dynamics in CD8(+) TILs reinforce T

cell exhaustion. *Nat Immunol*, 2020. **21**(12): p. 1540–1551.

12. Scharping, N.E., et al., Mitochondrial stress induced by continuous stimulation under hypoxia rapidly drives T cell exhaustion. *Nat Immunol*, 2021. **22**(2): p. 205–215.
13. Gulen, M.F., et al., cGAS-STING drives ageing-related inflammation and neurodegeneration. *Nature*, 2023. **620**(7973): p. 374–380.
14. Victorelli, S., et al., Apoptotic stress causes mtDNA release during senescence and drives the SASP. *Nature*, 2023. **622**(7983): p. 627–636.
15. Cao, K., et al., Mitochondrial dynamics regulate genome stability via control of caspase-dependent DNA damage. *Dev Cell*, 2022. **57**(10): p. 1211–1225.e6.
16. Veatch, J.R., et al., Mitochondrial dysfunction leads to nuclear genome instability via an iron-sulfur cluster defect. *Cell*, 2009. **137**(7): p. 1247–58.
17. Liu, Y., et al., Caenorhabditis elegans pathways that surveil and defend mitochondria. *Nature*, 2014. **508**(7496): p. 406–410.
18. Clouaire, T., et al., The THAP domain of THAP1 is a large C2CH module with zinc-dependent sequence-specific DNA-binding activity. *Proc Natl Acad Sci U S A*, 2005. **102**(19): p. 6907–12.
19. Lee, C.S., T. Lu, and G. Seydoux, Nanos promotes epigenetic reprograming of the germline by down-regulation of the THAP transcription factor LIN-15B. *Elife*, 2017. **6**.
20. Ma, X., X. Gou, and H. Zhang, T16G12.6/IMPORTIN 13-mediated cytoplasm-to-nucleus transport of the THAP transcription factor LIN-15B controls autophagy and lysosome function in C. elegans. *Autophagy*, 2025. **21**(8): p. 1779–1790.
21. Rolland, S.G., et al., Compromised Mitochondrial Protein Import Acts as a Signal for UPR(mt). *Cell Rep*, 2019. **28**(7): p. 1659–1669.e5.
22. Dillin, A., et al., Rates of behavior and aging specified by mitochondrial function during development. *Science*, 2002. **298**(5602): p. 2398–401.
23. Zecchini, V., et al., Fumarate induces vesicular release of mtDNA to drive innate immunity. *Nature*, 2023. **615**(7952): p. 499–506.

24. Yu, C.-H., et al., TDP-43 Triggers Mitochondrial DNA Release via mPTP to Activate cGAS/STING in ALS. *Cell*, 2020. **183**(3): p. 636–649.e18.
25. Bahat, A., et al., Ribonucleotide incorporation into mitochondrial DNA drives inflammation. *Nature*, 2025. **647**(8090): p. 726–734.
26. Wu, Z., et al., Mitochondrial DNA Stress Signalling Protects the Nuclear Genome. *Nat Metab*, 2019. **1**(12): p. 1209–1218.
27. Sutandy, F.X.R., et al., A cytosolic surveillance mechanism activates the mitochondrial UPR. *Nature*, 2023. **618**(7966): p. 849–854.
28. Kaur, N., et al., TECPR1 is activated by damage-induced sphingomyelin exposure to mediate noncanonical autophagy. *Embo j*, 2023. **42**(17): p. e113105.
29. Boyle, K.B., et al., TECPR1 conjugates LC3 to damaged endomembranes upon detection of sphingomyelin exposure. *Embo j*, 2023. **42**(17): p. e113012.
30. Thurston, T.L., et al., Galectin 8 targets damaged vesicles for autophagy to defend cells against bacterial invasion. *Nature*, 2012. **482**(7385): p. 414–8.

Methods

C. elegans strains

SJ4100 (zcIs13[*hsp-6p::GFP*]), MQ887 (*isp-1(qm150)*), MT1806 (*lin-15A(n767)*), SJ4005 (zcls4[*hsp-4p::GFP*]), CL2070 (dvIs[*hsp-16.2p::GFP*]), SJZ328(foxSi75 [*eft-3p::tomm-20::mKate2::HA*]), SJZ47 (foxSi16 [*myo-3p::tomm-20::mKate2::HA*]), EG7828(oxTi310 [*eft-3p::tdTomato::H2B*]), MT13232 (*lin-65(n3441)*), and N2 wild-type were obtained from the Caenorhabditis Genetics Center (Minneapolis, MN). VC3201 (*atfs-1(gk3094)*) was obtained from the National BioResource Project (Tokyo, Japan). The *lin-15B(jef48)* allele (g.15726178_15726632del) was generated in this study. The following extra-chromosomal arrays and integrated strains were generated in this study: MAT260 (jefIs20[*hsp-6p::GFP::hsp-6 3´UTR*]), MAT261 (jefIs21[*lin-15Bp::lin-15B::flag::unc-54 3´UTR; myo-2p::mCherry::unc-54 3´UTR*], MAT262 (jefIs22[*lin-15Bp::lin-15B::gfp::flag::unc-54 3´UTR; myo-*

2p::mCherry::unc-54 3´UTR]), MAT263 (jefIs23[*lin-15Bp::lin-15B*^{MTSmut}*::flag::unc-54 3´UTR; myo-2p::mCherry::unc-54 3´UTR*]), MAT264 (jefIs24[*lin-15Bp::lin-15B*$^{\Delta MTS}$*::gfp::flag::unc-54 3´UTR; myo-2p::mCherry::unc-54 3´UTR*]), MAT265 (jefIs25[*lin-15Bp::lin-15B*^{MTSmut}*::gfp::flag::unc-54 3´UTR; myo-2p::mCherry::unc-54 3´UTR*]), MAT266 (jefIs26[*lin-15Bp::lin-15B*$^{\Delta AT\text{-}hook1}$*::gfp::flag::unc-54 3´UTR; myo-2p::mCherry::unc-54 3´UTR*]), MAT267 (jefIs27[*lin-15Bp::lin-15B*$^{\Delta AT\text{-}hook2}$*::gfp::flag::unc-54 3´UTR; myo-2p::mCherry::unc-54 3´UTR*]), MAT268 (jefIs28[*lin-15Bp::lin-15B*$^{\Delta 1221\text{-}1440}$*::flag::unc-54 3´UTR; myo-2p::mCherry::unc-54 3´UTR*]), MAT277 (jefIs29[*lin-15Bp::lin-15B*$^{\Delta MTS}$*::flag::unc-54 3´UTR; myo-2p::mCherry::unc-54 3´UTR*]), MAT269 (jefEx67[*myo-3p::gfp::unc-54 3´UTR; myo-2p::mCherry::unc-54 3´UTR*], MAT270 (jefEx68[*myo-3p::lin-15B 351-400::gfp::unc-54 3´UTR; myo-2p::mCherry::unc-54 3´UTR*]), MAT271 (jefEx69[*myo-3p::lin-15B(C. brenneri) 344-393::gfp::unc-54 3´UTR; myo-2p::mCherry::unc-54 3´UTR*]), MAT272 (jefEx70[*myo-3p::lin-15B(C. remanei) 338-387::gfp::unc-54 3´UTR; myo-2p::mCherry::unc-54 3´UTR*]), MAT273 (jefEx71[*myo-3p::* α1^{mut}*::gfp::unc-54 3´UTR; myo-2p::mCherry::unc-54 3´UTR*]), MAT274 (jefEx72[*myo-3p:: linker*^{mut}*::gfp::unc-54 3´UTR; myo-2p::mCherry::unc-54 3´UTR*]), MAT275 (jefEx73[*myo-3p::*α2^{mut}*::gfp::unc-54 3´UTR; myo-2p::mCherry::unc-54 3´UTR*]), MAT276 (jefEx74[*myo-3p::* α1/2^{mut}*::gfp::unc-54 3´UTR; myo-2p::mCherry::unc-54 3´UTR*])

Transgenesis

Extra-chromosomal arrays were generated by standard microinjection into the germline. The injection mix typically contained the plasmid of interest (50 ng/µL) and a co-injection marker, *myo-2p::mCherry* (5 ng/µL). To create stable lines, extra-chromosomal arrays were integrated by X-ray irradiation and subsequently backcrossed at least five times with N2 before using for further analyses. For *lin-15B* expression constructs, a ~2.5 kb *lin-15B* promoter fragment and the *lin-15B* cDNA were cloned into a pBSK vector.

738 **Cell culture and transfection**

739 HEK293T cells were obtained from ATCC and cultured in Dulbecco's modified
740 Eagle's medium (DMEM) supplemented with 10% (v/v) fetal bovine serum (FBS).
741 Cells were grown at 37 °C in a humidified incubator with 5% CO_2. Transient
742 transfection of HEK293T cells was performed using polyethylenimine (PEI).
743
744 **RNA interference RNAi experiments and genome-wide RNAi screen**
745 RNAi clones were obtained from either the Vidal library or the Ahringer library.
746 RNAi bacterial strains were seeded onto NGM plates with 1 mg/mL IPTG (NGM-
747 IPTG) to induce double-stranded RNA (dsRNA) expression. Synchronized L1 larvae
748 were placed on RNAi plates and cultured at 20 °C. For double RNAi, equal volumes
749 of the two bacterial cultures were mixed before seeding.
750 The genome-wide RNAi screen was performed using the Vidal library. For the
751 screen, synchronized *isp-1 (qm150);hsp-6p::GFP* L1 larvae were placed on individual
752 RNAi plates. On day-1 of adulthood, worms were screened for suppression of *hsp-*
753 *6p::GFP* fluorescence.
754
755 **Reverse-transcription qPCR (RT-qPCR)**
756 Total RNA was extracted from L4-stage worms with indicated treatments and
757 genotypes using the RNeasy Plus Micro Kit (74034, QIAGEN). First-strand cDNA
758 was synthesized from the purified RNA using the LunaScript RT SuperMix Kit
759 (E3010, NEB). RT-qPCR was performed using Luna Universal qPCR Master Mix
760 (M3003, NEB). Primers used for RT-qPCR are listed in Extended Data Table 5.
761
762 **Analyses of UPR^{mt} induction**
763 Synchronized L1 worms carrying *hsp-6p::GFP* reporter were raised on plates seeded
764 with RNAi bacteria targeting mitochondrial components used in this study, including
765 *cco-1*, *hsp-6*, *spg-7*, *tim-23*, and *atp-1*. At the Day1 adult stage, the expression of *hsp-*
766 *6p::GFP* reporter was imaged. For endogenous *hsp-6* mRNA measurement, RNA was
767 extracted at the L4 stage and quantified by reverse-transcription qPCR (RT-qPCR).

Primers used are listed in Extended Data Table 5.

Induction of UPR^{ER} and heat shock response (HSR)

For induction of UPR^{ER}, synchronized L4-stage worms carrying *hsp-4p::GFP* were incubated in M9 buffer containing 25 ng/uL tunicamycin for 4 hours, after which they were transferred to fresh plates and cultured for additional 12 hours. The expression of the *hsp-4p::GFP* reporter was then imaged.

For induction of the heat shock response (HSR), synchronized L4-stage (40 h) worms carrying *hsp-16.2p::GFP* were heat-shocked at 34 °C for 30 minutes, followed by a 20-hour incubation at 20 °C. The expression of the *hsp-16.2p::GFP* reporter was then imaged.

Mitochondrial isolation and detection of LIN-15B mitochondrial localization

To assess the association of LIN-15B with mitochondria, an affinity purification of intact mitochondria was performed with minor modifications to a previously described protocol [31]. Approximately 25,000 synchronized L1 larvae foxSi75[*eft-3p::tomm-20::mKate2::HA*] worms carrying the indicated LIN-15B transgenic were grown on either *cco-1* RNAi or RNAi control bacteria at 20 °C. Worms were collected at day-1 adult stage and washed three times with 15 ml M9 buffer in a 15 ml tube, followed by one wash with 15 ml ddH_2O. Then the worms were transferred to a pre-chilled 2 ml Dounce homogenizer and resuspended in 2 ml ice-cold PBS supplemented with Protease Inhibitor Cocktail (78442, Thermo Scientific) followed by homogenization on ice with 100 gentle strokes. A small aliquot (60 µL) was saved as the whole-cell lysate (Input). The remaining homogenate was then cleared of debris and nuclei by sequential centrifugation at 200g and 1,000g. The resulting post-nuclear supernatant was incubated with pre-washed anti-HA magnetic beads (88837, Thermo Scientific) for 1 hour at 4°C with rotation (10 rpm). After washing three times with PBS, beads were boiled in 60 µL SDS sample buffer to elute bound complexes. Samples were then boiled at 100 °C for 10 min and analyzed by western blotting to detect LIN-15B and markers for mitochondrial, cytosolic, and nuclear compartments.

To validate the specificity of the mitochondrial enrichment and rule out non-specific binding of LIN-15B to the beads, a detergent solubilization control was performed in parallel. Prior to immunoprecipitation with anti-HA bead, the post-nuclear supernatant was treated with 1% Triton X-100 for 30 min on ice to solubilize all organellar membranes. Insoluble material was removed by centrifugation at 20,000g, and the resulting supernatant was then subjected to the same anti-HA immunoprecipitation procedure described above. The absence of LIN-15B co-purification under these conditions would confirm its specific association with intact mitochondrial structures.

Proteinase K (PK) protection assay

A crude mitochondrial fraction was prepared from approximately 150,000 synchronized day-1 adult *lin-15Bp::lin-15B::flag* transgenic worms previously cultured on control or *cco-1* RNAi plates. Day-1 adult worms were collected, washed twice with 15 mL M9 buffer, and once with ddH_2O, then transferred to a 5-mL Dounce homogenizer and resuspended in 5 mL ice-cold mitochondrial isolation buffer (50 mM KCl, 110 mM mannitol, 70 mM sucrose, 0.1 mM EDTA, 5 mM Tris-HCl pH 7.4) supplemented with protease inhibitor cocktail (78442, Thermo Scientific), and homogenized on ice with 100 gentle strokes. The homogenate was cleared of debris and nuclei by two sequential centrifugations at 1,000 g at 4 °C for 10 min. Mitochondria were pelleted by centrifugation at 10,000g at 4 °C for 10 min. This mitochondrial pellet was washed twice by resuspension in fresh mitochondria isolation buffer followed by re-pelleting at 10,000g.

The final mitochondrial pellet was resuspended in 1 mL ice-cold PBS, and equal aliquots (100 µL) of the mitochondrial suspension were incubated with the indicated concentrations of proteinase K (SAE0009, Sigma-Aldrich) for 30 min on ice. Proteolysis was terminated by adding PMSF to a final concentration of 1 mM and immediately mixing with 5× SDS sample buffer. Sample were boiled at 100 °C for 10 min and analyzed by western blotting.

Western blotting

Worm lysates or eluted samples were mixed with 5× SDS sample buffer. The samples were boiled for 10 min and then subjected to electrophoresis on SurePAGE Bis-Tris gels (GeneScript). Western blot analysis was performed on PVDF membranes after blocking with 5% BSA or milk. The blots were incubated with primary antibodies overnight at 4 °C, followed by incubation with secondary antibodies for 2 h. Blots were then visualized using an enhanced chemiluminescence (ECL) substrate and detected by a digital chemiluminescence imager.

DNA pull down assay

Two types of biotinylated DNA bait were prepared. For the full-length bait, an ~11 kb mitochondrial DNA (mtDNA) fragment was PCR-amplified using a 5' biotinylated primer (see Extended Data Table 5) and purified. For shorter fragments (biotin-DNA-1/2/3/4), complementary biotinylated forward and reverse oligonucleotides were synthesized commercially (see Extended Data Table 5) and annealed. The respective biotinylated DNA baits (50 µg of long mtDNA or 500 pmol of shorter) were coupled to 1 mg of streptavidin magnetic beads by overnight incubation at 4°C. The DNA-coupled beads were then washed with lysis buffer (20 mM Tris-HCl pH 7.5, 150 mM NaCl, 1 mM EDTA, 1% Triton X-100, supplemented with Protease Inhibitor Cocktail (78442, Thermo Scientific).

One 10-cm dish of HEK293T cells expressing the indicated protein was harvested and lysed by sonication in lysis buffer. Cell debris was removed by centrifugation at 20,000g. The supernatant was then incubated with 300 µg of the prepared biotin-DNA-streptavidin beads (or streptavidin beads alone as a negative control) for 6–8 hours at 4°C with rotation (10 rpm). The beads were then washed three times with 1.5 mL ice-cold lysis buffer at 4 °C for 10 min each with rotation (10 rpm). Bound proteins were eluted by directly resuspending the beads in 60 µL of SDS sample buffer, followed by boiling at 100 °C for 10 min. Eluted samples were analyzed by western blotting.

Formaldehyde crosslinking-based protein-DNA Immunoprecipitation and qPCR analysis

120,000 synchronized day-1 adult *lin-15Bp::lin-15B::gfp::flag* transgenic worms, previously cultured on control or cco-1(RNAi) plates, were harvested and crosslinked with 4% formaldehyde in PBS for 1 hour at 4°C. The reaction was quenched with 0.125 M glycine. The worms were centrifuged at 700g, the supernatant was removed, and the pellet was washed twice with PBS. The worms were then transferred to a pre-chilled 2 mL Dounce homogenizer and resuspended in 2 mL ice-cold PBS supplemented with Protease Inhibitor Cocktail (78442, Thermo Scientific). Worms were homogenized on ice with 100 gentle strokes. A 60 µL aliquot of worm lysate was retained as the qPCR reference template. The remaining lysate was centrifuged at 4 °C at 200g for 5 min and then at 1,000g for 10 min to remove debris and nuclei. To prepare soluble protein-mtDNA complex, the cleared supernatant was supplemented with Triton X-100 to a final concentration of 1% for 20 minutes at 4°C to solubilize membrane components, then centrifuged at 20,000g. The supernatant was then divided into two equal aliquots and incubated separately with mouse anti-Flag antibody (F1804, Sigma-Aldrich**)** or mouse IgG (15381, Sigma-Aldrich) for 4 hours at 4 °C, followed by incubation with protein A/G magnetic beads for 2 hours. These beads were subjected to stringent washes, first with Wash Buffer 1 (0.1% SDS, 1% Triton X-100, 2 mM EDTA, 150 mM NaCl, 20 mM Tris-Cl, pH 7.5) and then with buffer 2 (0.1% SDS, 1% Triton X-100, 2 mM EDTA, 400 mM NaCl, 20 mM Tris-Cl, pH 7.5). The protein-DNA crosslinking complexes were decrosslinked in 50 µg/mL proteinase K solution (dissolved in PBS) at 60 °C for 2 hours. The retained 60 µL whole-worm lysates was subjected to the same decrosslinking treatment. DNA was extracted using the DNeasy Blood & Tissue Kit (69506, QIAGEN) and subsequently analyzed by qPCR. Nuclear genomic DNA (*rpl-28*) from whole-worm lysates serve as the reference template. Primers used for qPCR are listed in Extended Data Table 5.

Quantification of Cytosolic mtDNA by qPCR

Approximately 15,000 L1 larvae worms were raised on plates seeded with indicated

RNAi bacteria and collected at L4-stage. The worms were washed three times with PBS, then transferred to a pre-chilled 2 mL Dounce homogenizer and resuspended in 1 mL isolation buffer (150 mM NaCl and 50 mM HEPES). Worms were homogenized on ice with 100 gentle strokes. 60 µL of lysate was retained, and total DNA was extracted from it to serve as the subsequent qPCR reference template. The lysate was centrifuged at 20,000g at 4 °C for 10 min and the supernatant was further filtered through a 0.22 µm filter to obtain the cytosolic fraction. DNA was extracted from the cytosolic fractions and the retained whole-worm lysates using DNeasy Blood & Tissue Kit (69506, QIAGEN) according to the manufacturer's instructions. mtDNA in the cytosolic fractions were quantified by qPCR using primers targeting mtDNA regions. Nuclear genomic DNA (*rpl-28*) from whole-worm lysates serve as the reference template (primers are listed in Extended Data Table 5).

Transmission electron microscopy (TEM) and immunogold TEM

Samples for TEM were prepared using a high-pressure freezing and freeze-substitution (HPF/FS) protocol as previously described [32]. Samples were prepared by high-pressure freezing standard protocol. In brief, worms were transferred into 200 µL PBS containing 20% (w/v) bovine serum albumin and immediately high-pressure frozen using a Leica EM ICE. Freeze-substitution was performed in a Leica EM AFS2 device in acetone containing 1% osmium tetroxide, 0.1% uranyl acetate and 10% methanol for 6 days. After substitution, samples were warmed to -20 °C and washed with pure acetone. Infiltration was carried out with increasing concentrations of Epon resin in acetone (25% for 30 min, 33% for 3.5 h, 50% overnight, 75% for 4 h, and four times (6 h each) in 100% Epon resin). The samples were embedded in a mold and polymerized at 60 °C for 48 h. Ultrathin sections (70 nm) were cut on a Leica EM UC7 ultramicrotome, mounted on formvar-coated copper grids. For standard ultrastructural analysis, sections were post-stained with 2% uranyl acetate followed by Sato's triple lead stain. For immunogold labeling, sections were incubated with mouse anti-DNA antibody (CBL186, Sigma-Aldrich), followed by incubation with 12 nm colloidal gold-conjugated goat anti-mouse secondary antibody (115-205-166,

Jackson). Images were acquired on a Talos L120C TEM (Thermo Fisher Scientific).

Microscopy and image analysis

For imaging of the *hsp-6p::GFP*, *hsp-4p::GFP* and *hsp-16.2p::GFP* reporters, day-1 animals were immobilized in M9 buffer containing 100 µg/mL levamisole and mounted on NGM plates. Fluorescence images were acquired using Nikon SMZ18 stereomicroscope, and the mean GFP fluorescence intensity was quantified using ImageJ software.

For imaging and quantification of nuclear LIN-15B::GFP, day-1 animals were similarly immobilized with 100 µg/mL levamisole in M9 buffer and mounted on 2% agarose pads on glass slide. Images were captured on a Zeiss LSM980 confocal microscope using a 20x objective. The mean GFP fluorescence intensity within intestinal nuclei was then quantified.

For imaging of live HEK293T cells, images were acquired using a Zeiss LSM800 confocal microscope with a 63x objective.

RNA sequencing and analysis

Worms were grown for 48 h on EV or *cco-1* RNAi bacteria, followed by RNA sequencing performed by BGI (Shenzhen, China). Raw reads were quality filtered using SOAPnuke [33], aligned to the reference genome (WBcel235) using Bowtie2 [34], and gene expression levels were quantified with RSEM [35]. Differentially expressed genes (DEGs) were identified using DESeq2 ($Q \leq 0.05$) [36]. Functional enrichment analysis for Gene Ontology (GO) and KEGG pathways was performed on the resulting DEG lists using a hypergeometric test. Data visualization was performed using Dr. Tom platform provided by BGI.

Lifespan assays

Lifespan assays were performed at 20°C. Synchronized L1 worm were raised on plates seeded with the corresponding bacteria and cultured without 5-fluoro-2’deoxyuridine (FUdR). Starting on day 1 of adulthood, worms were transferred to

fresh plates every two days throughout their reproductive period to separate them from their progeny. Survivorship was scored daily, with worms considered dead if they failed to respond to gentle prodding with a platinum wire. Lifespan data were analyzed using the Kaplan-Meier method combined with the log-rank (Mantel-Cox) test via the online tool OASIS2.

Statistics and reproducibility

Unless indicated otherwise, statistical analyses were performed using GraphPad Prism 10.2. The methods for calculating P-values were described in the figure legend corresponding to each dataset. $P < 0.05$ was considered statistically significant. Details regarding reproducibility are provided in the figure legends for each data. The results were consistent across all replicates.

31. Ahier, A., et al., Affinity purification of cell-specific mitochondria from whole animals resolves patterns of genetic mosaicism. *Nat Cell Biol*, 2018. **20**(3): p. 352–360.
32. Manning, L. and J. Richmond, High-Pressure Freeze and Freeze Substitution Electron Microscopy in C. elegans. *Methods Mol Biol*, 2015. **1327**: p. 121–40.
33. Li, R., et al., SOAP: short oligonucleotide alignment program. Bioinformatics, 2008. **24**(5): p. 713–4.
34. Langmead, B. and S.L. Salzberg, Fast gapped-read alignment with Bowtie 2. *Nat Methods*, 2012. **9**(4): p. 357–9.
35. Li, B. and C.N. Dewey, RSEM: accurate transcript quantification from RNA-Seq data with or without a reference genome. *BMC Bioinformatics*, 2011. **12**: p. 323.
36. Love, M.I., W. Huber, and S. Anders, Moderated estimation of fold change and dispersion for RNA-seq data with DESeq2. *Genome Biol*, 2014. **15**(12): p. 550.

Acknowledgment We thank the Caenorhabditis Genetics Center and Y.T. (Institute of Genetics and Development, Chinese Academy of Sciences) for providing *C. elegans* strains. We also acknowledge the Microscopy Core and other facilities at Westlake University for their support, and we thank Limin Zheng, Linxi Wang, Fang Xiao, and Yinping Gao for their technical assistance with microscopy. This work was supported by the National Natural Science Foundation of China (No. 32530030, No. 32350015, and No. 32070565), the Zhejiang Provincial Natural Science Foundation of China (XHD24C0701, QN25C070004, LQ23C040002), by State Key Laboratory of Gene Expression, the HRHI program (No. 202209003 and No. 202109007) of the Westlake Laboratory of Life Sciences and Biomedicine, the Westlake Center for Genome Editing (No.21200000A992510/004), the Westlake Education Foundation of Westlake University and the Zhejiang Provincial Key Laboratory Construction Project.

Author Contributions Y.W. and H.T. conceptualized the study; Y.W. designed and performed the experiments, analyzed the data, and wrote the manuscript; H.T. supervised the study and edited the manuscript.

Fig. 1

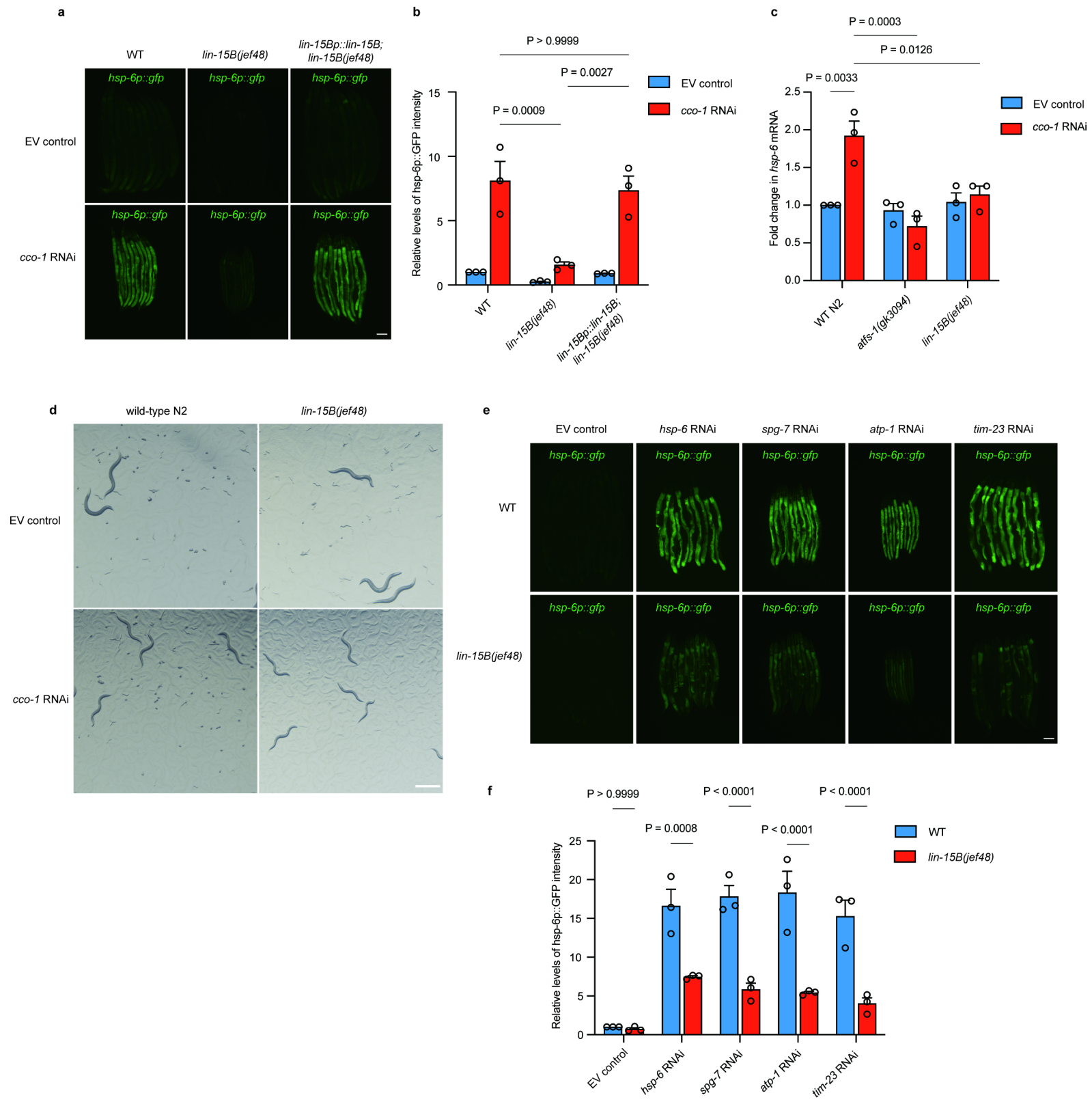

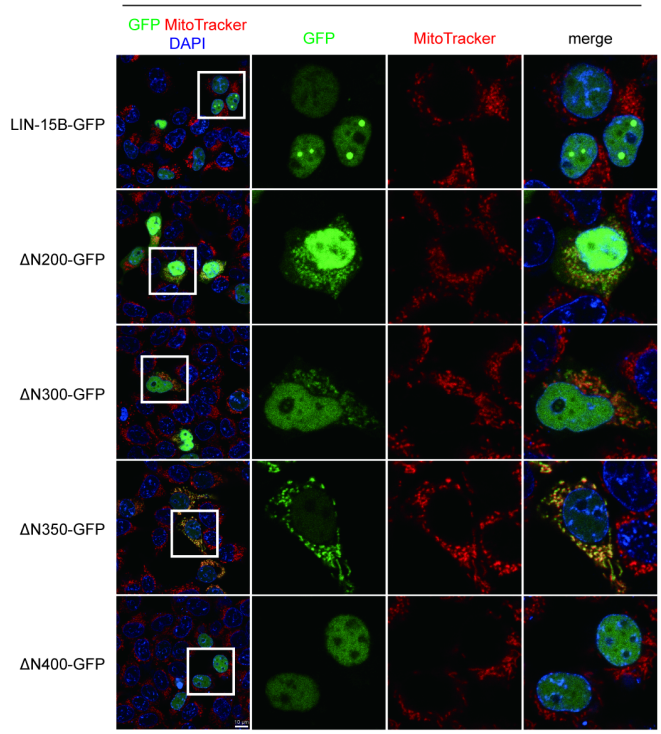

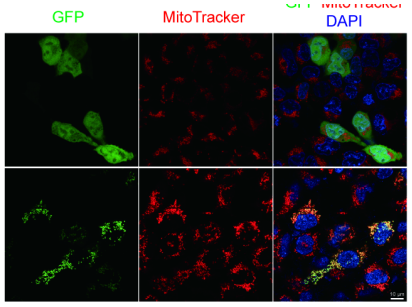

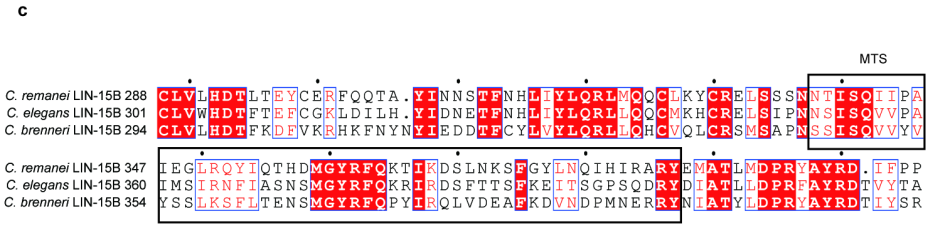

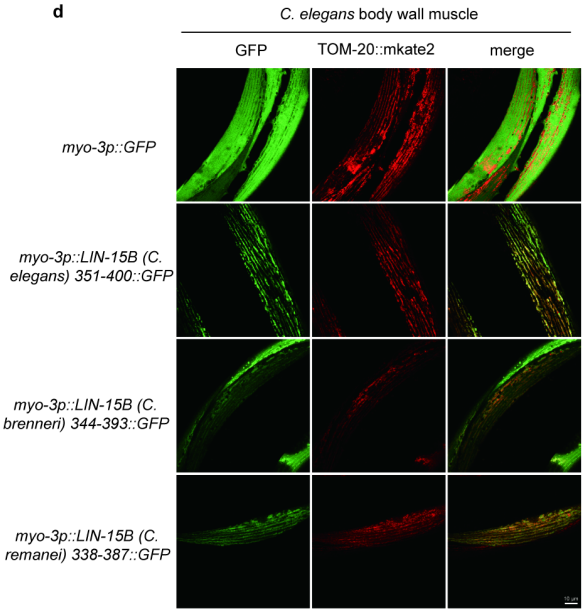

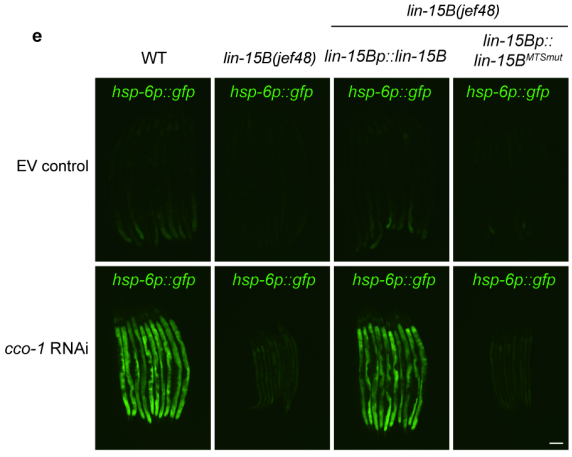

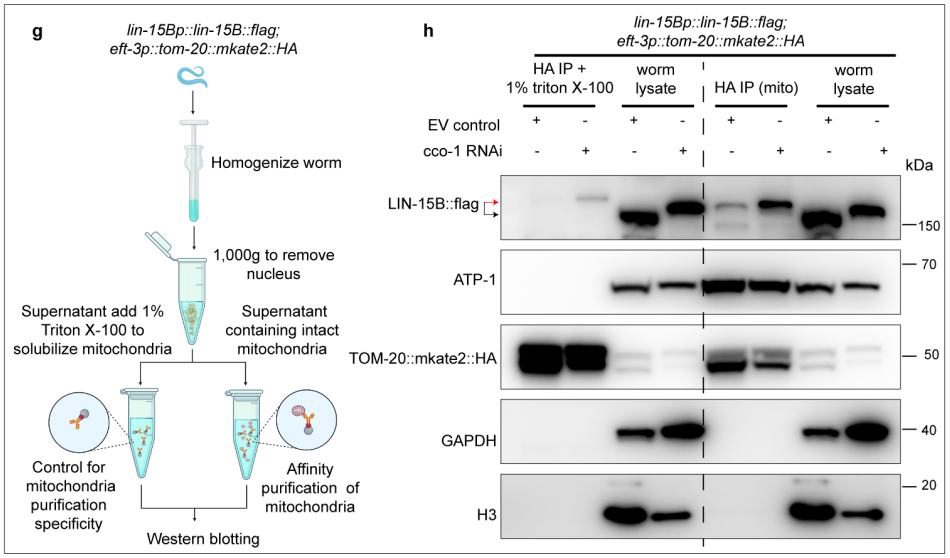

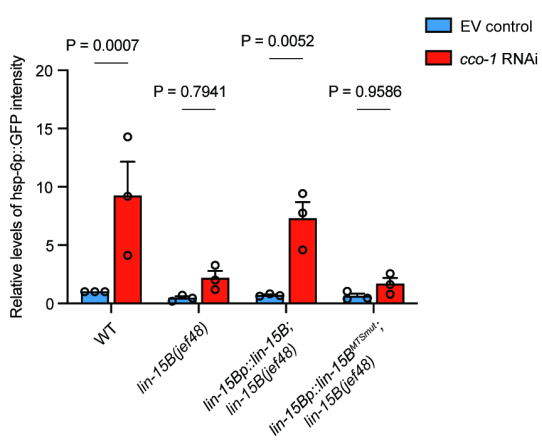

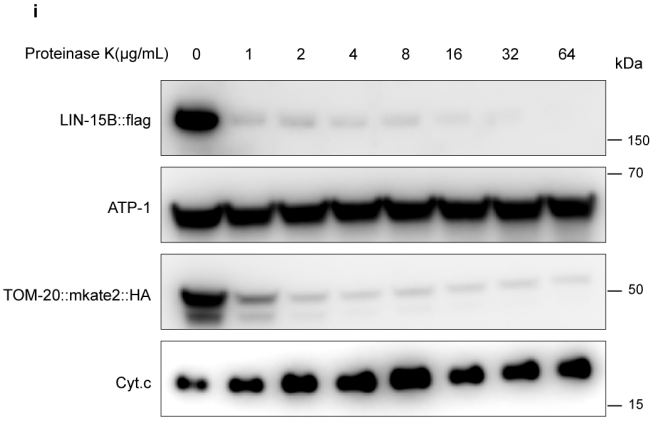

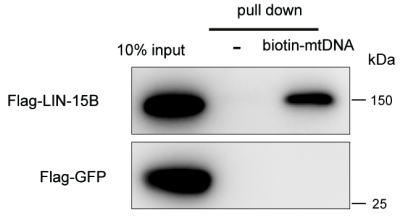

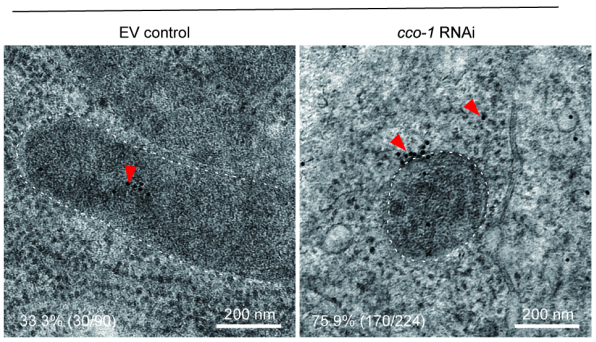

b

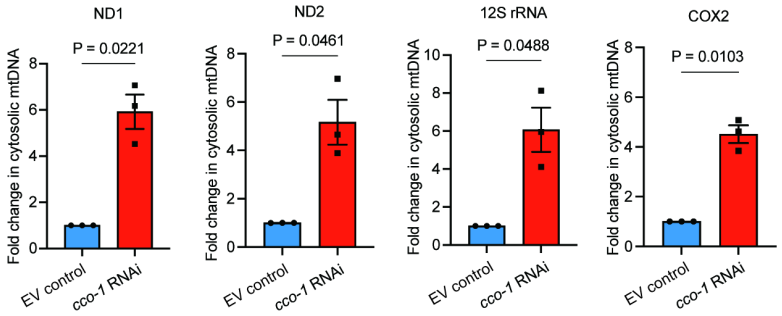

c

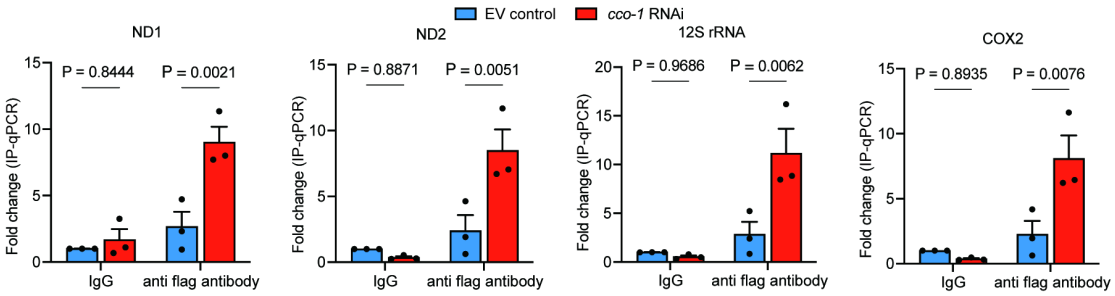

e

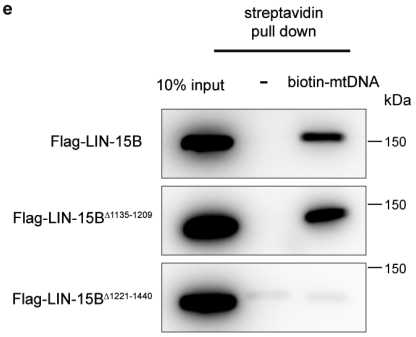

f

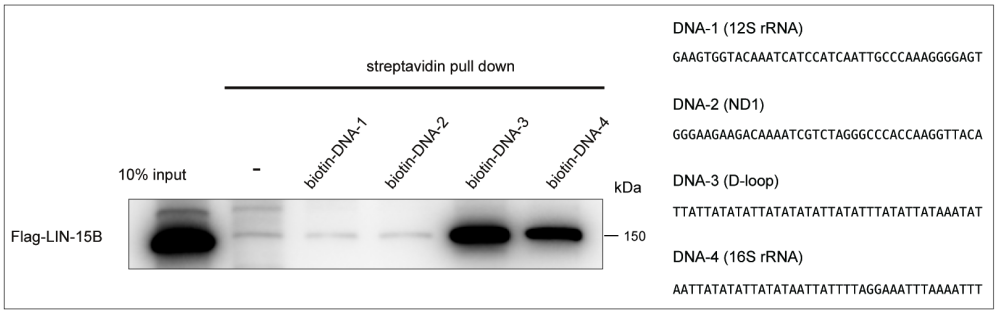

g

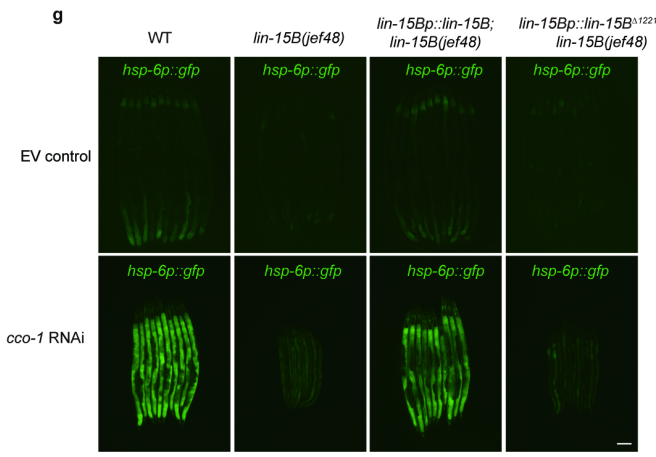

h

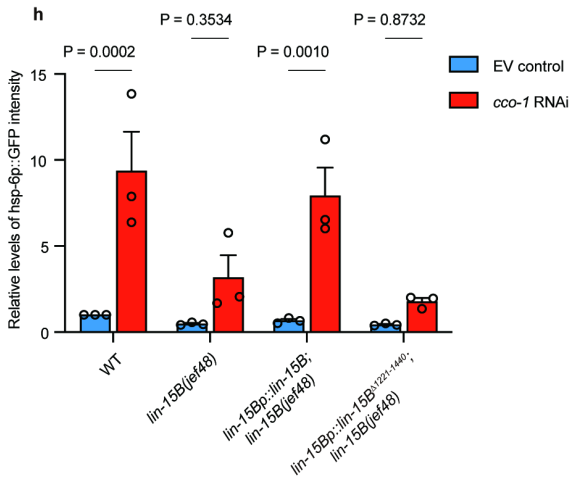

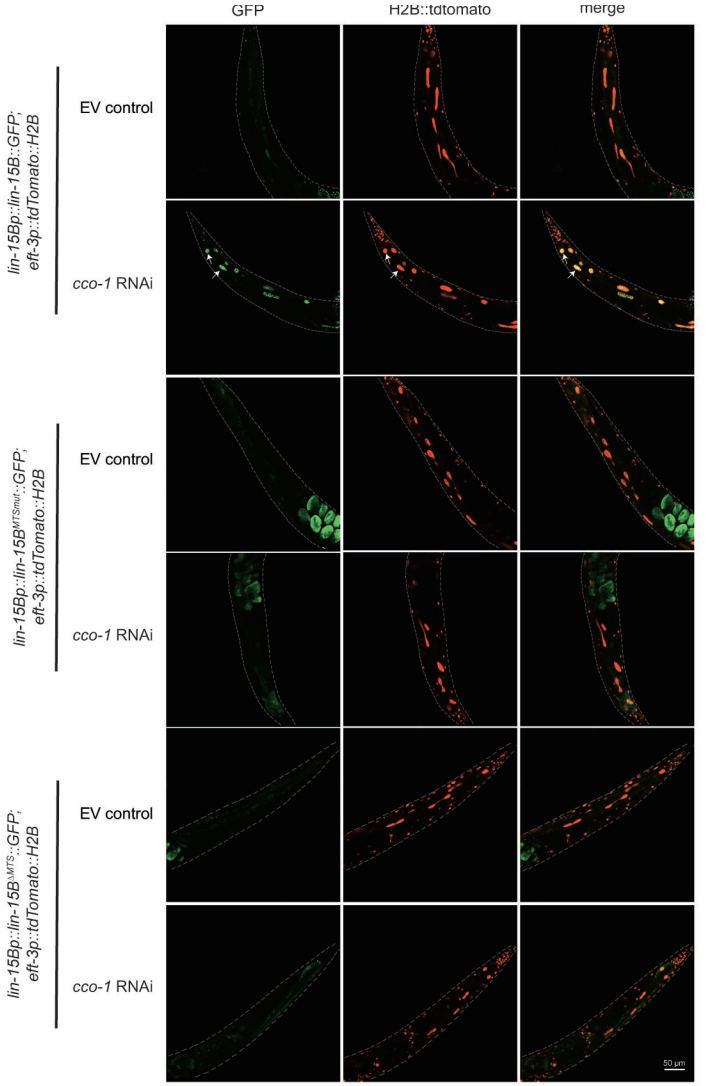

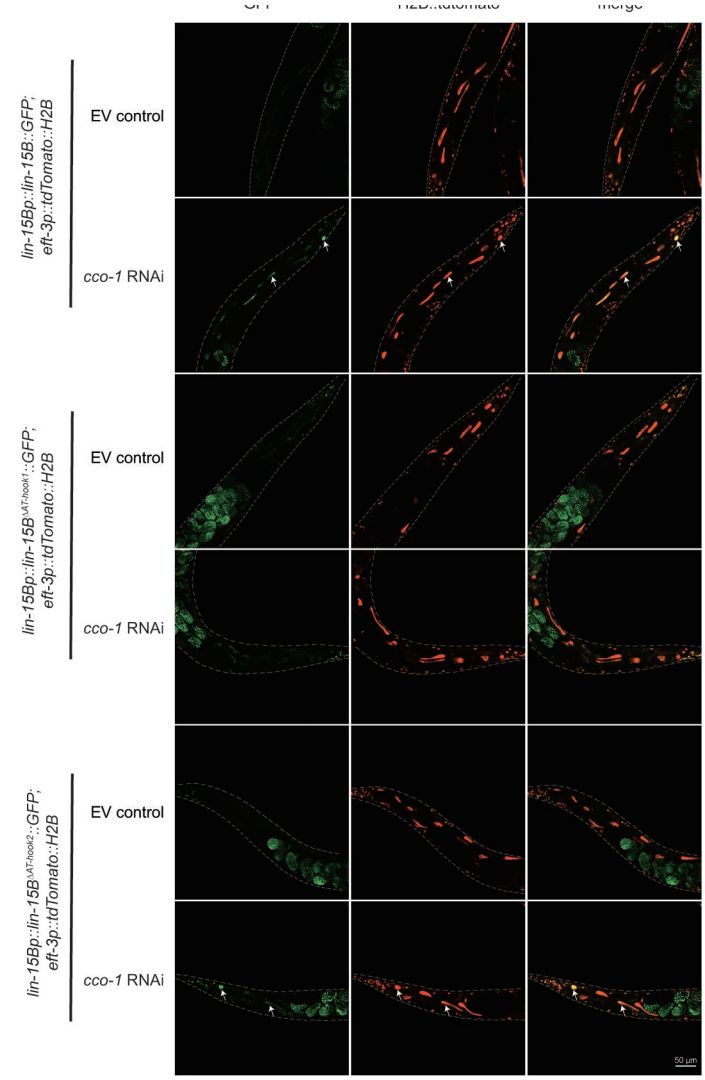

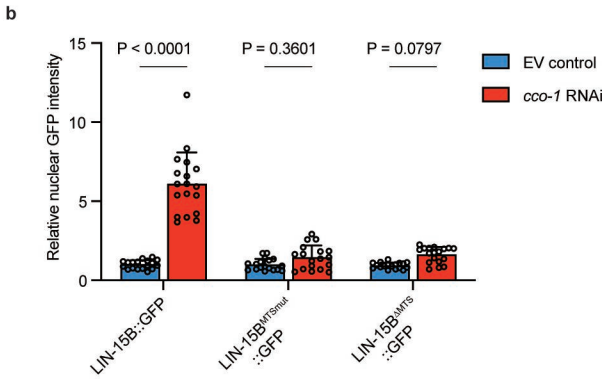

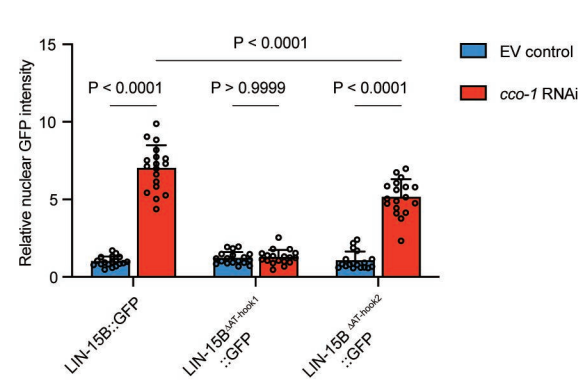

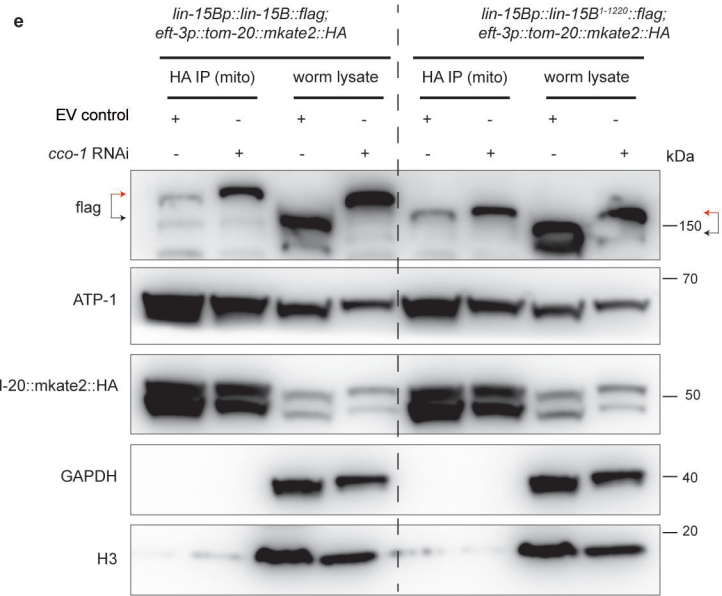

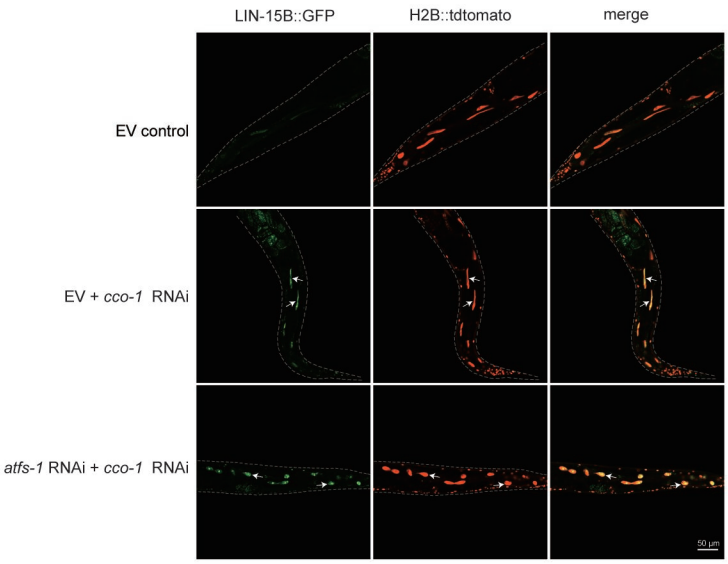

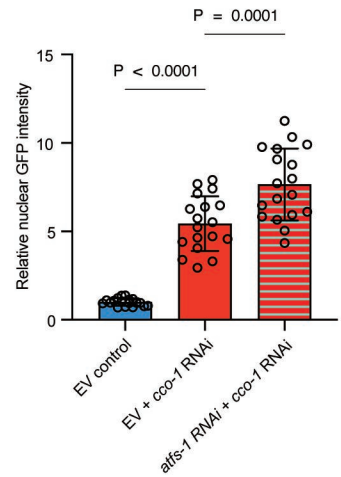

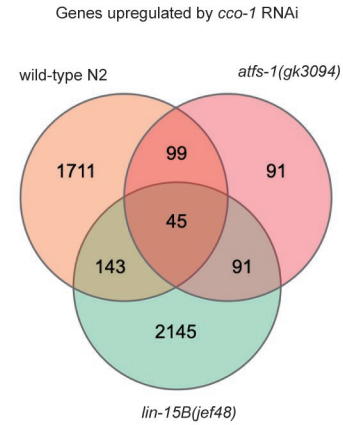

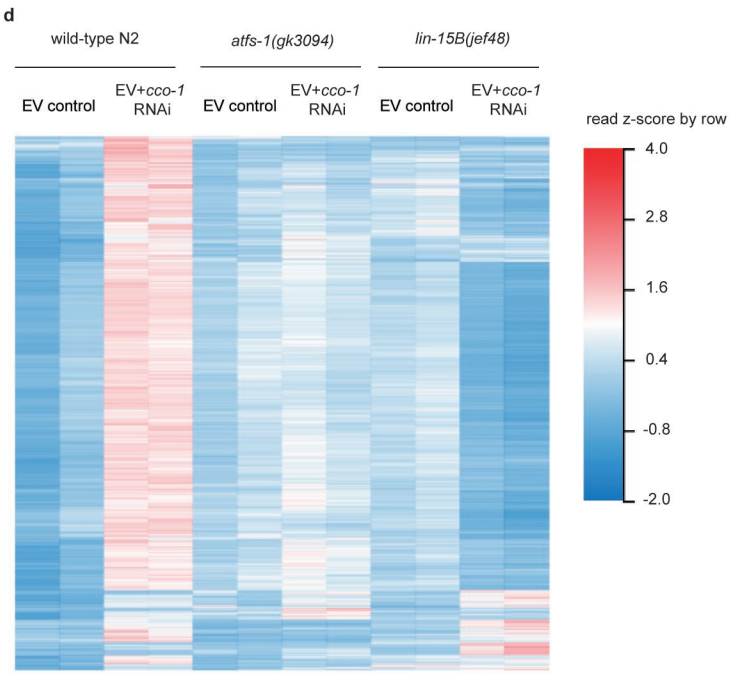

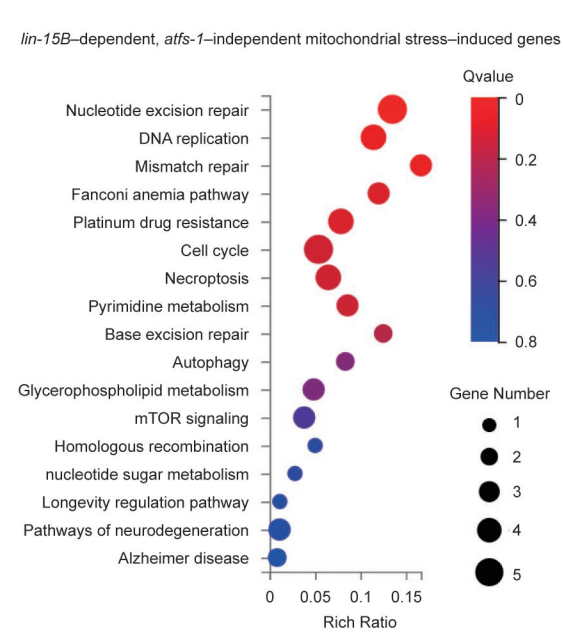

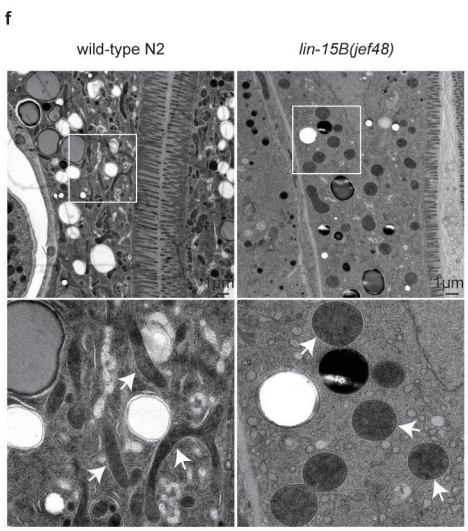

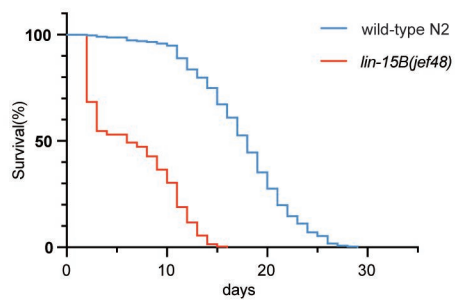

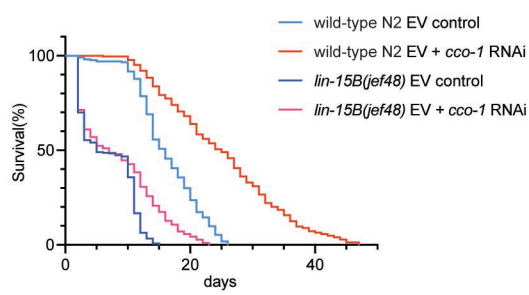

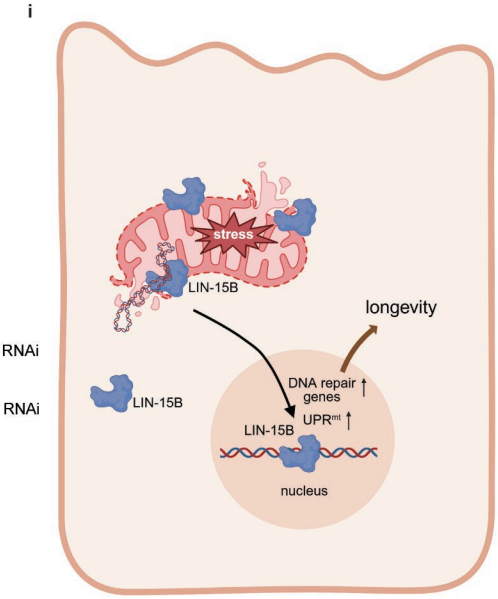

Extended Data Fig. 1

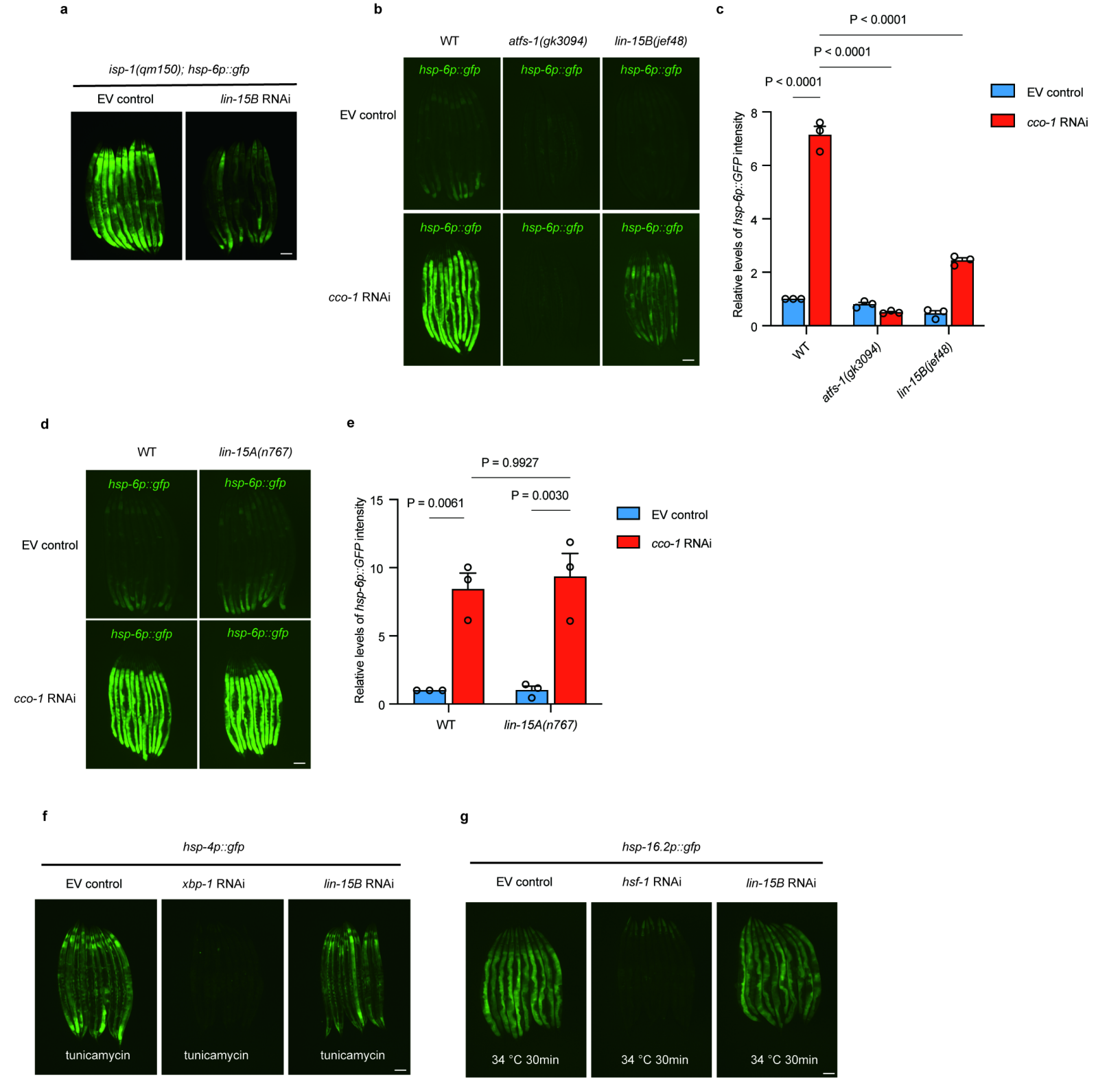

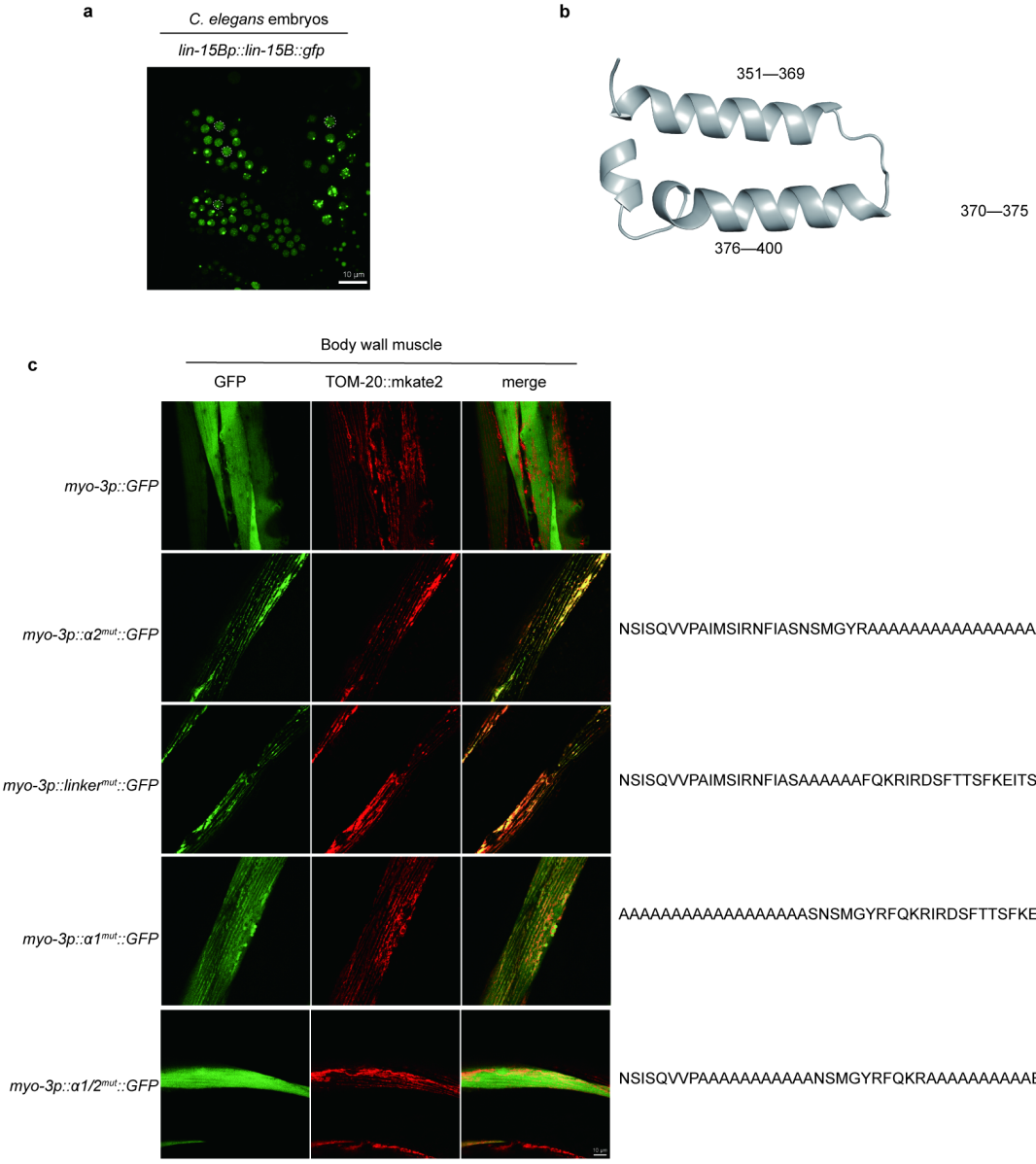

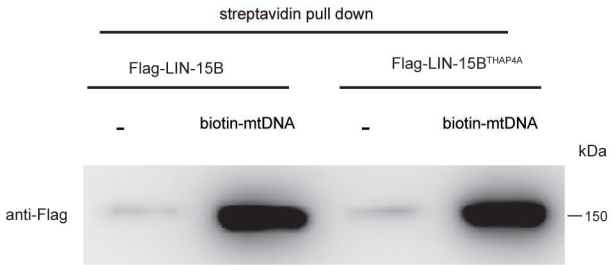

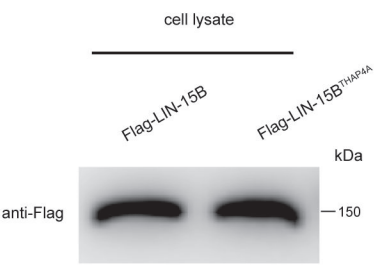

Extended Data Fig. 4

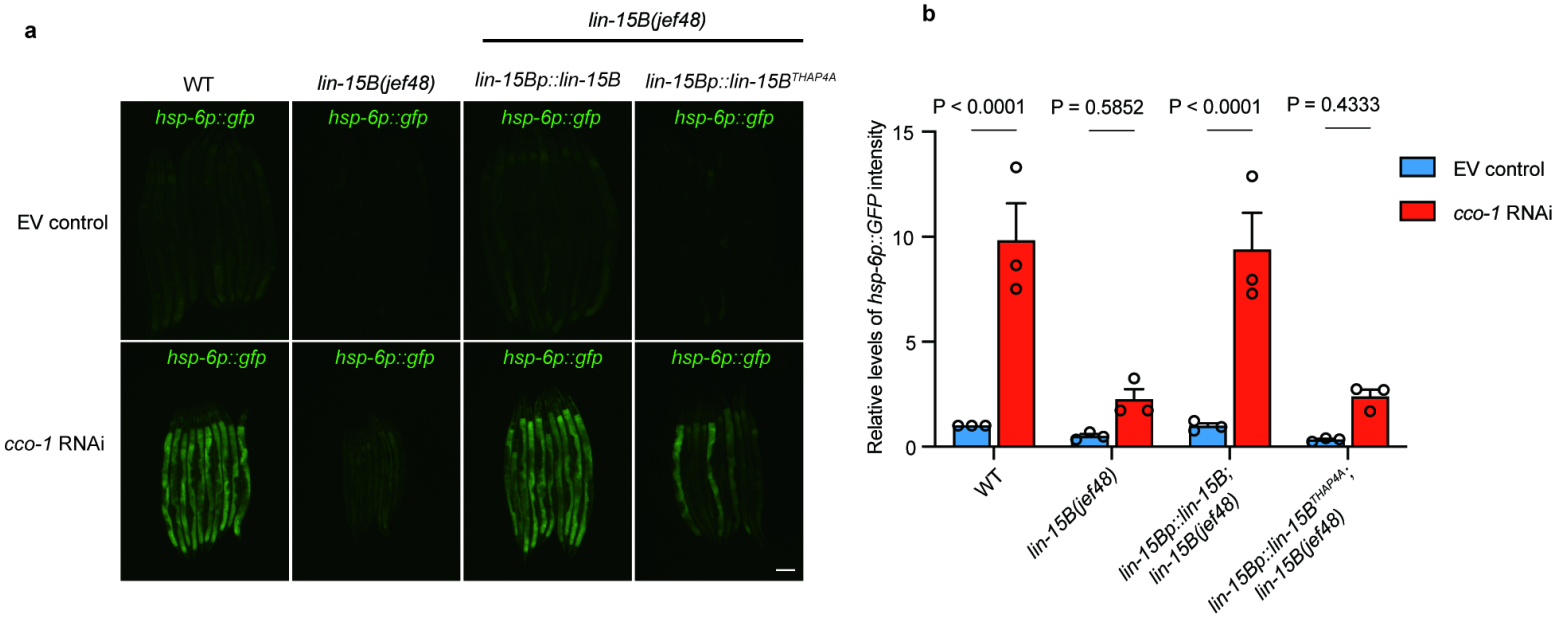

Extended Data Fig. 5

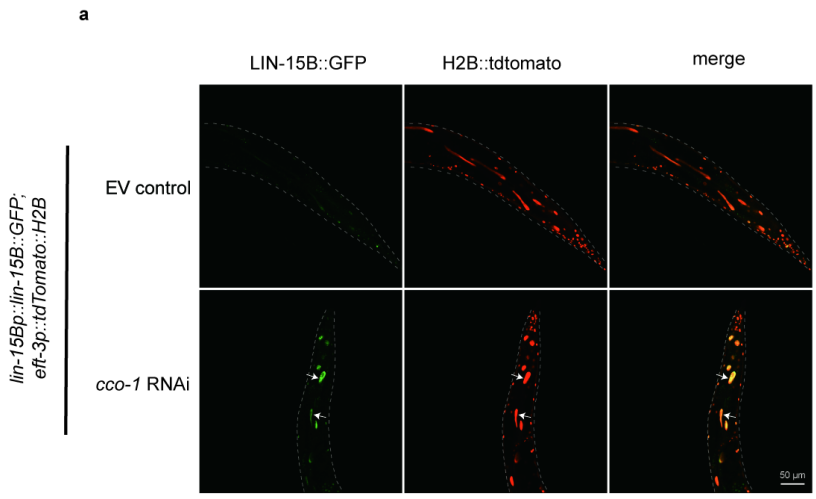

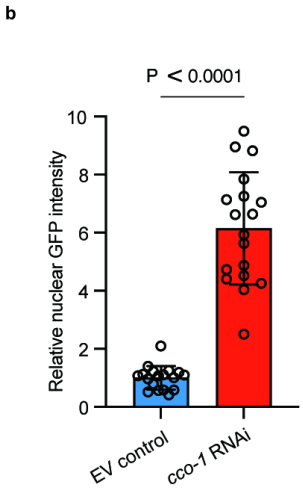

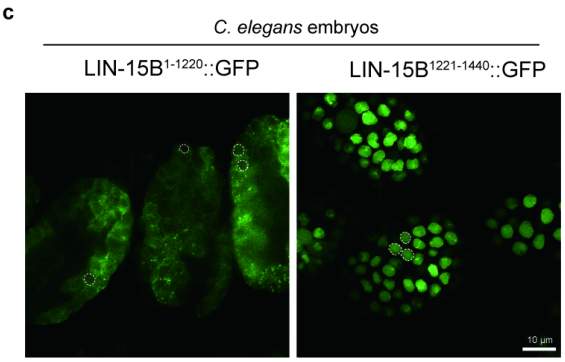

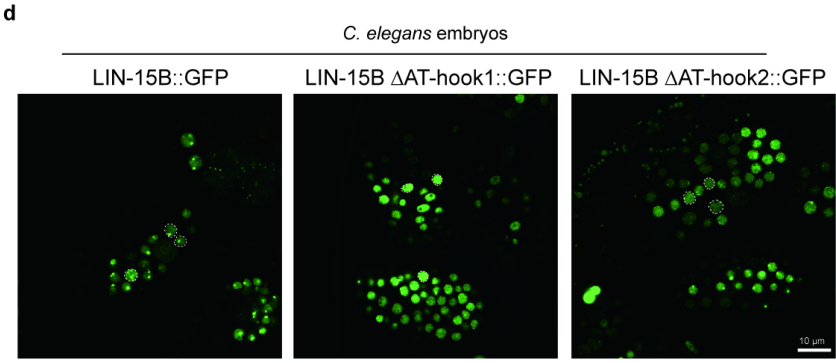

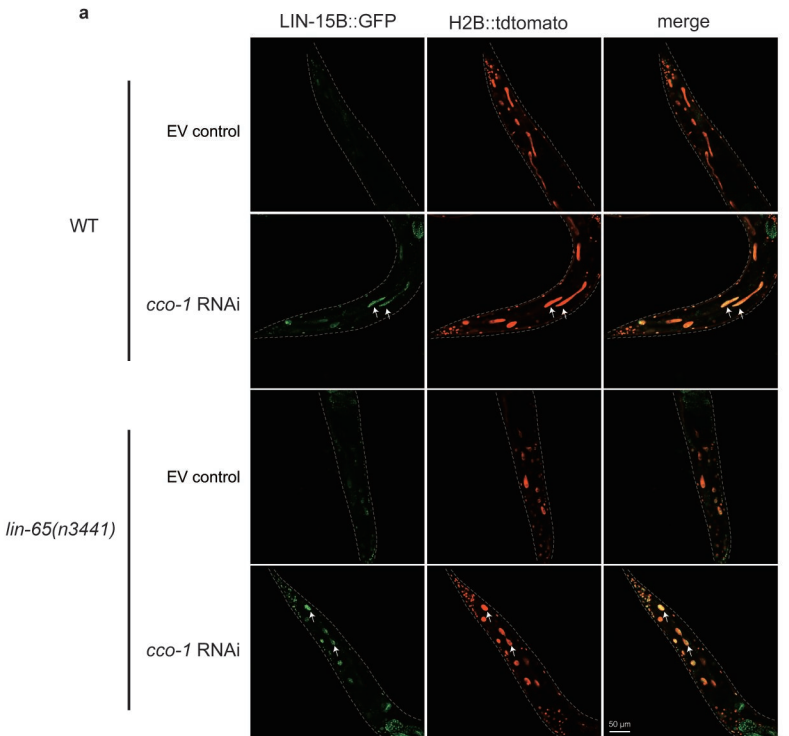

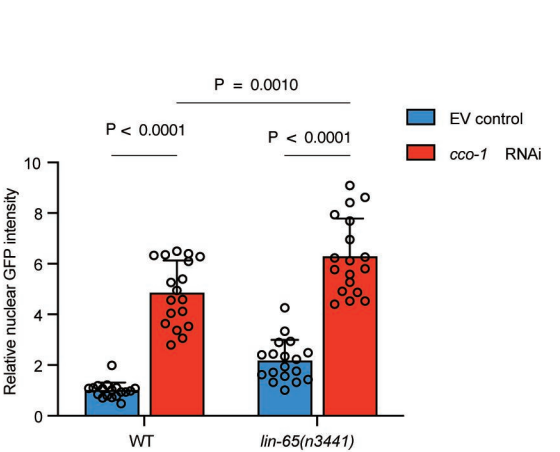

Extended Data Fig. 7